SIMULATION OF THREE DIMENSIONAL CURRENT SPREADING IN PHOTONIC CRYSTAL VCSEL STRUCTURES

A Thesis
Presented to
The Academic Faculty

by

Aditya Kulkarni

In Partial Fulfillment
of the Requirements for the Degree
Master of Science in the
School of Electrical and Computer Engineering

Georgia Institute of Technology
3rd December 2008

SIMULATION OF THREE DIMENSIONAL CURRENT SPREADING IN PHOTONIC CRYSTAL VCSEL STRUCTURES

Approved by:

Dr Benjamin Klein, Advisor
School of Electrical and Computer Engineering
Georgia Institute of Technology

Dr Ian Ferguson
School of Electrical and Computer Engineering
Georgia Institute of Technology

Dr David Citrin
School of Electrical and Computer Engineering
Georgia Institute of Technology

Date Approved: 1st December 2008

To my parents,

"Ours is but to reason why"

ACKNOWLEDGEMENTS

I would first like to express my immense gratitude to my Advisor,Dr Benjamin Klein, who provided me with an opportunity to conduct research and also proved the Advisor rumors totally wrong. I would also like to thank Dr Alexey Maslov of Canon USA. His constant help and guidance have been very important factors during the entire course of my research. I express my gratitude to Dr P.D.Yoder, Anusha and Sriraman for the help and support they have provided. I would like to thank my friend Vivek. This work would not have begun without him. I would also like to thank Fahad for all the delicacies that my appetite has enjoyed. Finally, to everybody else who was there, in good times and bad, Thank you.

TABLE OF CONTENTS

DEDICATION iii

ACKNOWLEDGEMENTS iv

LIST OF TABLES vii

LIST OF FIGURES viii

SUMMARY x

I INTRODUCTION 1

1.1 Lasers and VCSELs 1

1.2 Simulation: requirement and methodology 3

1.2.1 Need for simulation 3

1.2.2 Simulation techniques 4

1.2.3 Simulation tools 6

1.3 Three dimensional simulation 7

1.3.1 Discretisation of device geometry 7

1.3.2 Modular approach to 3D simulation 11

II FORMULATION AND IMPLEMENTATION 14

2.1 Physical model 14

2.1.1 Current Continuity 14

2.1.2 Active region model 19

2.2 Coupling and Newton's method 26

2.2.1 Newton's method 28

2.3 Implementation and algorithms 33

2.3.1 Bulk transport and coupling to active region and cavity . . 33

2.3.2 Voltage stepping and iterative solutions 35

2.3.3 Active resistor model 35

III RESULTS 39
3.1 Validation of continuity equation 39
3.1.1 Linear resistor - Prism 39
3.1.2 Linear resistor - Spherical quadrant 41
3.2 Validation of the active resistor model 47
3.2.1 Simple diode with large electrodes 47
3.2.2 Modeling Symmetrical structures 50
3.3 VCSEL modeling 50
3.4 Photonic crystal VCSEL structures with defects 59
3.5 Analysis of band to bound recombination model 59
3.6 Performance analysis of the simulator 61
IV CONCLUSION 64
4.1 Future Work 64
4.1.1 k.p.model 65
4.1.2 Drift-Diffusion model 65
4.1.3 Efficient optical solver 66
REFERENCES 68
VITA 74

LIST OF TABLES

1 Dimensions for the spherical structure 43
2 Dimensions for the diode structure 48
3 Dimensions for the VCSEL structure 53
4 Comparison of CPU times for different solves 62
5 CPU times for different number of nodes in the CPU solver 63

LIST OF FIGURES

1 Depiction of VCSELs and edge emitting lasers 2
2 Variations in VCSEL structure to reduce multiple transverse mode . . 3
3 Examples of symmetry in electronic applications 5
4 Comparison of triangular meshes in 2D 9
5 Delaunay and non Delaunay Tetrahedra 10
6 Three dimensional meshes 11
7 Depiction of the Active resistor model 13
8 2D mesh and voronoi areas 16
9 Depiction of 3D Voronoi volume 17
10 Calculation of partial areas in a tetrahedron 19
11 Orientations of triangles and tetrahedra 20
12 Active resistor Physical model 20
13 Active resistor formulation 23
14 Active resistor functionality 26
15 1D formulation for the active resistor model 27
16 Illustration of the convergence of Newton's method in 1D 32
17 Top level flowchart for the simulator. Reading input data and cases of operation 34
18 Operation of the voltage loop and handling convergence in the simulator 36
19 Program flow for the Newton's method and calculation of the Jacobian and right hand side 37
20 Flowchart for active resistor update at each iteration 38
21 Rectangular prism with top and bottom electrodes : linear resistor . . 40
22 I-V curves for the linear device: Simulation and Analytical plots . . . 41
23 Relative error in current for the simulation of the linear device 42
24 Potential distribution in the device at V = 5.0 Volts 42
25 Iso surfaces for the potential at V = 0.5,1.5,2.5,3.5 and 4.5 Volts . . . 43

26 Discretised spherical structure 44

27 Potential distribution in the spherical structure 44

28 Iso surfaces in the spherical structure at V = 0.2,0.4,0.6 and 0.8 V . . 45

29 Potential distribution along the radial direction 46

30 Potential distribution for a geometry with hole 46

31 Structure used to for diode simulation 47

32 Inputs for the effective resistor model 48

33 I-V curves for the diode. Linear and Logarithmic scales 49

34 Laser diode, and half of the structure 50

35 Comparison of I-V and L-I curves for full and half diode 51

36 Simple VCSEL structure 51

37 $1/4^{th}$ of the VCSEL structure 52

38 Description of the $1/4^{th}$ VCSEL structure 53

39 Confinement factors for the $1/4^{th}$ VCSEL structure 54

40 I-V plots for the $1/4^{th}$ VCSEL structure 55

41 Plots of optical power for the VCSEL structure 55

42 Experimental I-V and L-I curves for similar VCSEL 56

43 Distribution of current density and carrier density on active layer . . 57

44 Comparison of current density above and below threshold 58

45 Photonic crystal VCSEL structure with holes 59

46 I-V plots for different defect dimensions 60

47 L-I curves for different A coefficients for the $1/4^{th}$ VCSEL structure . 61

48 Comparison of CPU time for DGESV and PARDISO solvers 62

49 Modular depiction of the 3D simulator 67

SUMMARY

An efficient simulation technique for calculating the current distribution in a Vertical Cavity Surface Emitting Laser (VCSEL) is proposed and implemented. The technique consists of a hybrid 1D/3D approach to the problem. The 3D aspect of simulation is essential for devices like a photonic crystal VCSEL where the existing 2D simulation techniques are inadequate. The modular approach of the technique is advantageous, as it provides flexibility in dealing with device simulations of varying complexity. It also provides a relatively short simulation time, beneficial for exploring a large design parameter space. The box integration technique is used for discretizing the equations and sparse matrix methods are used in solving the matrices. Simulation results and comparisons are provided for various aspects and modules of the simulator. The results for a few sample simulations indicate that the analysis has reasonable agreement with experimental results. The simulation error can be reduced using more accurate models for the active region of the laser.

CHAPTER I

INTRODUCTION

1.1 Lasers and VCSELs

Semiconductor lasers and LEDs are extensively used in a wide variety of applications such as lighting, data storage, telecommunications, optical sensors and displays. Advancements in crystal growth and device fabrication have led to an exploration of alternative laser designs and LED structures for increased efficiency. An interesting description of the development of the semiconductor laser can be found in [28]. The Vertical Cavity Surface Emitting Laser (VCSEL), which emits light perpendicular to the growth plane of the device, provides an attractive alternative to the conventional edge emitting lasers. VCSELs have significant advantages over their edge emitting Fabry Perot counterparts in many areas. The most prominent among these are the ease of fabrication and on wafer testing, which enable high volume and low cost manufacturing, and low drive currents; which enable low power devices. VCSELs have been used extensively for a wide variety of applications such as Gigabit Ethernet networks, and optical interconnects[17]. The origin of the VCSEL dates back to 1977, although extensive study and fabrication of VCSELs based on GaAs started in 1992[29]. A detailed discussion of the of the advantages and applications of the VCSEL can be found in [46] and manufacturing and fabrication are dealt with in [18]. More recently, Gallium Nitride VCSELs emitting in the blue - ultraviolet part of the spectrum are under extensive investigation.

A typical VCSEL structure is as shown in Figure 1. The mirrors of the VCSEL structure consist of stacks of semiconductor layers that form Distributed Bragg Reflectors (DBR). The gain medium in the VCSEL is similar to the gain medium of any

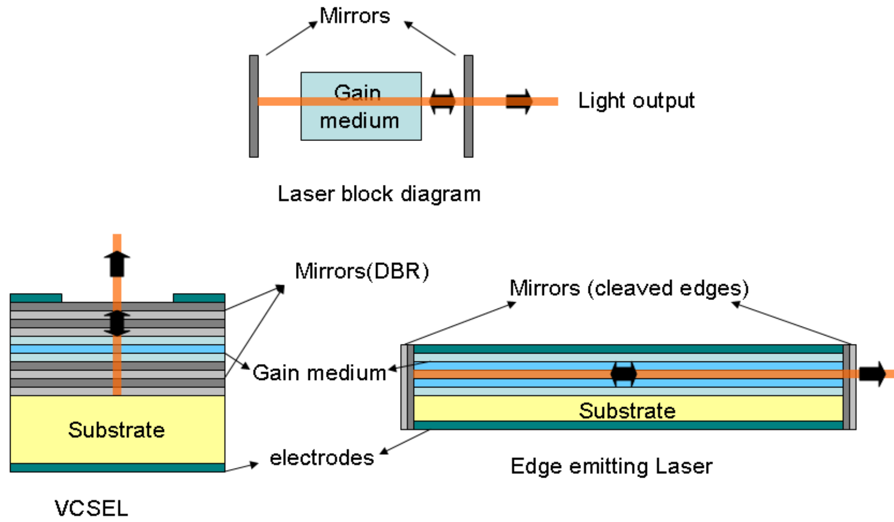

Figure 1: Depiction of VCSELs and edge emitting lasers

semiconductor laser; the heterojunctions between the narrow-bandgap well material and the wider-bandgap barrier material form a quantum well which enhances optical carrier recombination. In conjunction with the reflectors and an external pump, this enables sustained stimulated emission and hence coherent emission of light. We shall only deal with electrical pumping, which is used to maintain population inversion of carriers in the quantum well. The electrodes indicated in Figure 1 are used for this purpose.

Although VCSELs possess the advantages of low power consumption, high modulation speed and single longitudinal mode operation, most large aperture VCSELs simultaneously lase in multiple modes in the transverse direction. This is undesirable in applications such as optical sensors and optical communication, and can lead to loss of data due to modal dispersion[65]. Although single mode operation can be achieved using small optical apertures, these are limited to low power output. It is difficult to achieve single-mode operation with large apertures and higher power outputs. Variations on the standard VCSEL structure have been investigated to achieve single-mode operation at moderate power output. Prominent among these, are using

varying sizes for oxide apertures[65] and etching two-dimensional arrays of holes to create a photonic crystal defect cavity to serve as the lasing aperture[19], as shown in Figure 2.

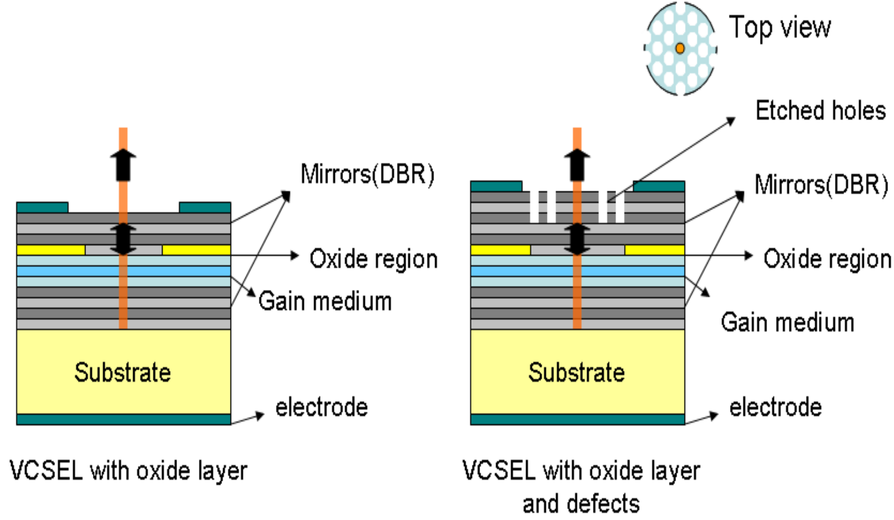

Figure 2: Variations in VCSEL structure to reduce multiple transverse mode

1.2 Simulation: requirement and methodology

1.2.1 Need for simulation

The detailed physics involved in the operation of semiconductor lasers cannot be accurately and predictively modeled analytically. The need for numerical methods and simulation techniques is quite evident in the case of VCSELs with 2D photonic crystal layers, where device symmetry cannot be used to reduce the three dimensional problem to one or two dimensions. In addition to the difficulty of calculating carrier transport in the device, which will be addressed in this thesis, solving for the optical modes is also a difficult task. The three dimensional vector Helmholtz equation is not separable for photonic crystal VCSELs with defects such as the one shown in Figure 2. Therefore, computational techniques are widely used to analyse these devices. Predictive simulation techniques provide an opportunity to obtain estimates of device performance before they are fabricated experimentally. Accurate simulation

methods also provide cost effective device design solutions without the need for blind trial and error using fabricated devices.

1.2.2 Simulation techniques

Computational methods for carrier transport simulation of semiconductor devices, have been used extensively since the work of Scharfetter and Gummel[52], which provides robust methods for discretising the drift-diffusion equations. One, two and three dimensional discretisation of the drift-diffusion equations [13] and the associated iterative methods [12] have been effectively used to date for simulations involving classical models. Various numerical techniques for the simulation of semiconductor devices are well-established in the literature [59, 53]. These also include simulations involving more sophisticated models, such as Hydrodynamic equations and Monte Carlo methods.

The methodology and choice of the 2D and 3D simulation techniques depends on the device under consideration and the physical models required to capture the device operation. The method of 2D simulation is valid when the physical parameters do not change dramatically along one of the spatial dimensions of the device. A large number of device geometries lie in this category and hence 2D simulation techniques have been utilised and improved rigorously.

The analysis of edge emitting quantum well lasers using 2D simulation methods is a well researched subject and significant literature is available on this topic[25, 26, 22, 23, 24]. The typical methodology used in these simulations is the geometrical discretisation of the cross section of the given structure, followed by applying varying physical models for the structure. The drift diffusion and continuity equations coupled with the Poisson equation are used for the entire device structure by discretising these equations in the 2D domain. Thermionic emission theory is used at the heterojuction interfaces where there is an abrupt change in the bandgap of the material. The

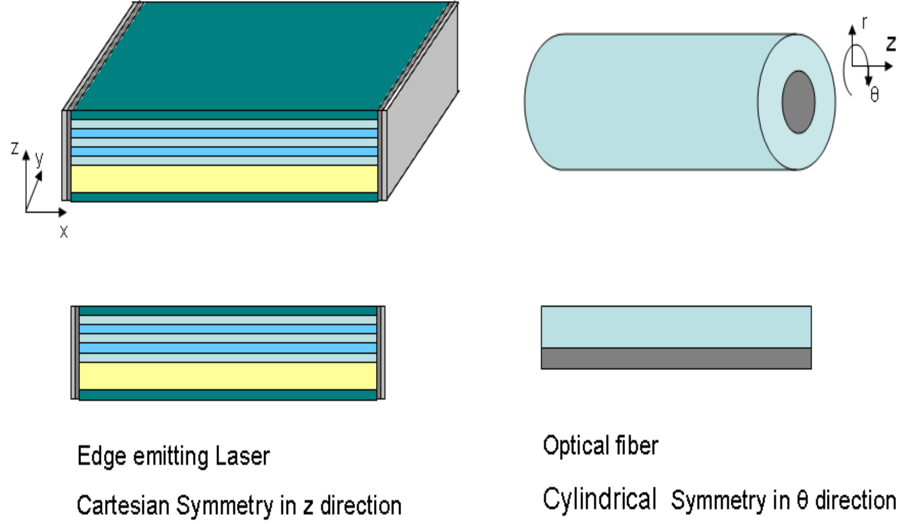

Figure 3: Examples of symmetry in electronic applications

Quantum well is analysed using a different approach, due to its intrinsically quantum mechanical nature. Recombination process, both radiative and non-radiative, are modeled to take account of the change in carrier density in the quantum well. The bound states (energy states) are obtained using the Schrodinger equation. Scattering mechanisms are also considered to determine the carrier capture rate from the classical to the quantum regions.

This model forms the essence of the 2D laser simulator MINILASE [25] and has also been used to simulate various VCSEL structures by exploiting the cylindrical symmetry in conventional VCSEL structures [49, 33, 32, 42, 39]. Numerical simulation of VCSELs has also been performed using other 1D and 2D simulation methods [58, 56] and also using quasi 3D methods[64, 45, 15, 43, 57]. Quasi 3D methods involve the 2D simulation of the device at various cross sections, and coupling these cross sections along the third dimension to obtain the entire 3D solution for the device. Quasi 3D models are useful if the device has gradual but non trivial changes in geometry and other characteristics in one dimension. Apart from this, full 3D simulation techniques of edge emitting lasers [64] and VCSELs [62] have also been

developed. They involve a similar approach to modelling as the 2D simulation with the quantum well and the bulk regions being modeled separately. The discretization of the equations is done in a 3D domain, hence increasing the complexity and simulation time.

1.2.3 Simulation tools

There are a variety of commercial tools available for device simulation with different types of physical models and numerical methods. The following simulation tools have been used extensively to model semiconductor laser diodes. The scope and limitations of each tool is described here.

1) **Minilase 2D laser simulator :** This is a 2D laser simulator from the University of Illinois[25]. It features a full 2D drift-diffusion carrier transport model for all regions, as well as thermionic emission over heterojunctions, an 8-band k.p model for the quantum well states, and gain calculation including many-body effects. It can be used for problems in rectangular and cylindrical coordinates, but it is limited to solving problems in 2D planes.

2) **LASTIP :** A 2D CAD laser simulator from Crosslight. It is used primarily to model edge emitting lasers and Quantum cascade lasers. LASTIP has similar features and limitations as Minilase.[1]

3) **PICS3D :** This is a quasi 3D device simulator from Crosslight[1]. In this case, the 3D device is split into a number of 2D slices and the equations are solved for the coupled slices. This is an improvement over a 2D model, but still requires a slowly-varying longitudinal direction. It also has a full 3D simulator, but the memory and computation time required is large.

4) **TCAD Sentaurus :** This is a diverse 3D simulator from Synopsys[8]. Apart from the cost factor, the drawback here is huge memory and computation time requirements for large sized 3D problems. This is also true of other fully 3D device simulators.

5) **DESSIS :** This is a device simulator from ISE AG. It is multi dimension simulator and can perform 1D,2D or 3D simulations. It is available as a part of the TCAD package from Synopsys. It has a wide variety of transport models ranging from the drift-diffusion equations to Monte-Carlo techniques. It is typically used for the modelling of semiconductor devices made from Silicon or III-V compounds like GaAs. DESSIS has been used for full 3D simulations of VCSELs and edge emitting lasers [64, 62]

6) **TiberCAD :** This is a 3D device simulator from the Opto and Nano Electronics group at the University of Roma.[10]. TiberCAD can be used to analyze various devices like lasers, LEDs, MOSFETs, HEMTs and Nanostructures. Apart from a wide range of models used for charge transport, it also incorporates a variety of physical aspects like strain, piezoelectric effect, pyroelectric effects[11].These are essential for the analysis of Nitride based materials, which are currently of high interest in semiconductor lasers. TiberCAD also performs multi dimensional device simulations and uses tetrahedral grids for 3D simulations.

1.3 Three dimensional simulation

1.3.1 Discretisation of device geometry

Although the 3D simulation method does not change the physics involved in the device, the exact numerical formulation of the problem is different and more involved

in comparison to the 2D case.One of the important challenges in three dimensional simulation techniques is the discretisation of the device geometry such that it is suitable for the matrix methods used to find the solutions. Since the analysis of lasers involves non linear equations, the discretised equations are solved using non linear iterative matrix methods such as the Newton's method, Jacobi-Davidsson method and so on. These iterative methods start from a initial guess and then try to approach the solution by linearizing the problem in each iteration. Since the direction of approach can change with every step, these methods are prone to instability and can diverge away from the solution. The geometry and discretisation form an important part of the stability criterion.The volumes and angles of the discretised elements contribute to the matrix coefficients. These coefficients determine the convergence of the iterative method.

The need for discretising arbitrary structures with arbitrary geometries implies that one has to consider non cuboidal elements in the grid generation. Tetrahedral grids have several advantages among the volumetric elements that can be chosen to build a mesh. The connectivity of tetrahedral grids is regular and leads to efficient storage. They are convenient to represent and due to the geometry of the tetrahedron, grids of varying resolutions can be created, while maintaining symmetric elements. The symmetry of triangular or tetrahedral elements implies that all angles are equal or almost equal. As long as obtuse angles are avoided, these elements will result in a well conditioned coefficient matrix.

Let us consider the 2D case for ease of visualisation. Figure 4 shows how the same set of points can be used to create two different meshes. The mesh on the left is a regular mesh, and is favourable for either the Finite Element Method (FEM) or box integration discretisation techniques that are used in this work. If the circumcircle of any triangle in the mesh does not contain any other point apart from the nodes of the triangle, the mesh is considered favourable. This criterion is called the Delaunay

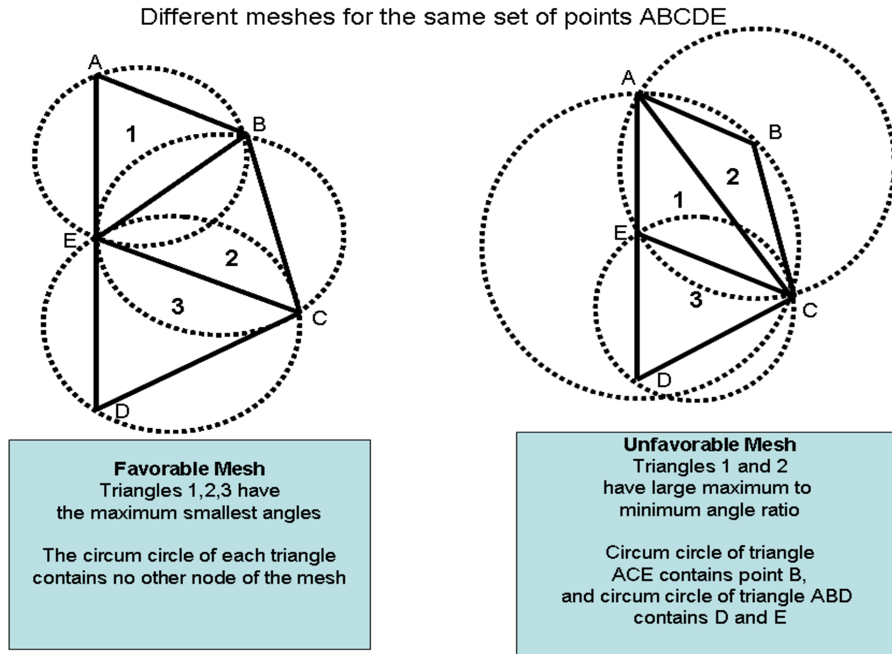

Figure 4: Comparison of triangular meshes in 2D

criterion[55]. If all the sub elements in the mesh also satisfy the Delaunay criterion, the entire mesh is said to be conforming Delaunay. In 2D, this implies that each edge is a chord of at least one circle which does not include other nodes. Such meshes have optimal properties[38]. As is evident from the figure, the mesh on the right side does not satisfy the Delaunay criterion. It can also be seen that the triangles of the mesh on the right side have large obtuse angles. It should be noted that for a given set of points, the Delaunay mesh is not unique. Also, certain set of points cannot be triangulated to produce a Delaunay mesh unless extra points are added to them. It is also beneficial if the generated meshes have a minimal number of points (unless the user specifies a high resolution mesh). Good mesh generators should not add an excess of additional points to achieve the Delaunay criterion. A similar discussion applies for desirable meshes in 3D. Most properties of Delaunay meshes and their optimality can be extended from 2D to higher dimensions[51].

The achievement of conforming Delaunay triangulation for a set of points in the

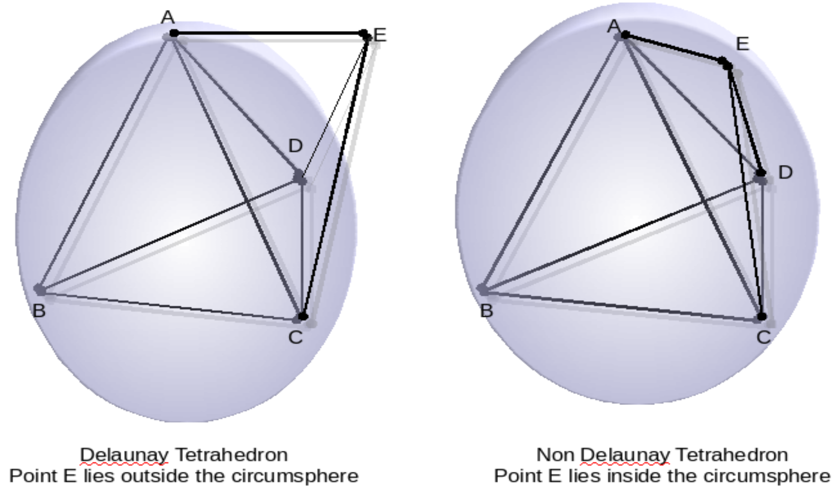

Figure 5: Delaunay and non Delaunay Tetrahedra

2D domain is guaranteed[21], but this is not the case for tetrahedralization in a 3D domain. The incremental flip algorithms used for generating Delaunay meshes are not guaranteed to terminate in 3D[30], especially for non-convex structures.Non convex structures are those where the shortest path between two points on the structure might lie outside the structure. Since laser device structures are likely to be non convex (e.g., holes in the VCSEL structure), the criterion for optimal meshes needs to be relaxed. Constrained Delaunay tertrahedralization is a satisfactory alternative as such tetrahedralizations possess most properties of conforming Delaunay tetrahedralizations [54, 16]. Constrained Delaunay tetrahedralization implies that the elements and sub elements on the boundaries of the domain are conforming Delaunay and the interior elements have circumcircles or circumspheres which do not enclose two vertices of the domain on the same side of the element facet, unless those two vertices belong to that element. An explanation of the constrained Delaunay tetrahedralization can be found in [16, 54]. The laser simulation method proposed here uses the box integration method for discretising the equations. Hence, it is imperative that the

mesh generator used to discretize the device produces constrained Delaunay tetrahedralisations. The mesh software 'Tetgen' developed by Hang Si at WIAS, Berlin[9] guarantees constrained Delaunay meshes for piecewise linear planar geometries. This tool is used for the generation of meshes for the device structures simulated in this thesis.

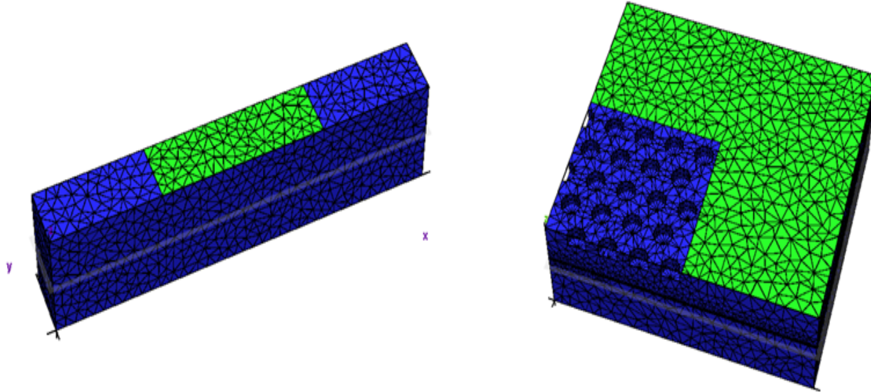

Constrained Delaunay tetrahedral meshes generated using Tetgen. The green regions form the electrode

Figure 6: Meshes generated in Tetgen

1.3.2 Modular approach to 3D simulation

As described in Section 1, most simulators model the gain region of the semiconductor laser in a different manner from the bulk of the device. The gain region, in our formulation, consists of the entire depletion region of the diode as well as several diffusion lengths on either side, and will include one or more quantum wells. In this region it is imperative to model a variety of physical processes that can be neglected in the rest of device, such as stimulated recombination. Quantum mechanical models, when used for modeling the physical processes in the laser, are mainly applied to the regions in and around the gain region. Even though the restriction of computationally intensive models to the gain region results in a reduction in simulation time, full 3D simulation still remains time consuming. The need for further approximations in the

simulation techniques with minimal compromise in accuracy has led to the research of other modular techniques.

Recent investigations of semiconductor LEDs and lasers focus on the important nitride material system. The nitride materials have larger bandgaps, which makes them very attractive for LEDs and lasers in the blue-UV region. The III-nitride devices, which are used in conjunction with the group III elements like Aluminium,Gallium and Indium are suitable for a variety of applications like lighting, data storage and display devices. The simulator described in this thesis takes advantage of the property of high current concentration near the electrodes when appropriate electrode configurations are used. This spatial localisation of current was also demonstrated using 3D simulation techniques for nitride materials[50]. This implies that away from the electrodes, the current density is primarily directed in the vertical direction in a vertical cavity structure. Since the gain region is away from the electrodes, the current through the gain region is primarily vertically directed, and can be modeled using a 1D simulation technique for each discretised point in the plane of the gain region, while using 3D techniques for the rest of the device. This hybrid 1D/3D approach was used by Evstratov et.al [20] in analyzing the current crowding effects in blue LEDs. The 1D model used in the active region of the LEDs is described in [31].

The model divides the entire plane of the gain region into a set of 'active resistors' which can be described by non linear equations. These equations provide a relation between the current density in each active resistor and the potential difference across each active resistor. This model can vary in complexity and hence provides flexibility in the accuracy versus computational time tradeoff. The bulk region is modelled using the drift current continuity equation (Laplace equation). Since this is a single equation for each discrete point, the size of the computation is greatly reduced compared to the full 3D drift-diffusion model. However, this technique does neglect asymmetric current spreading within the active region.

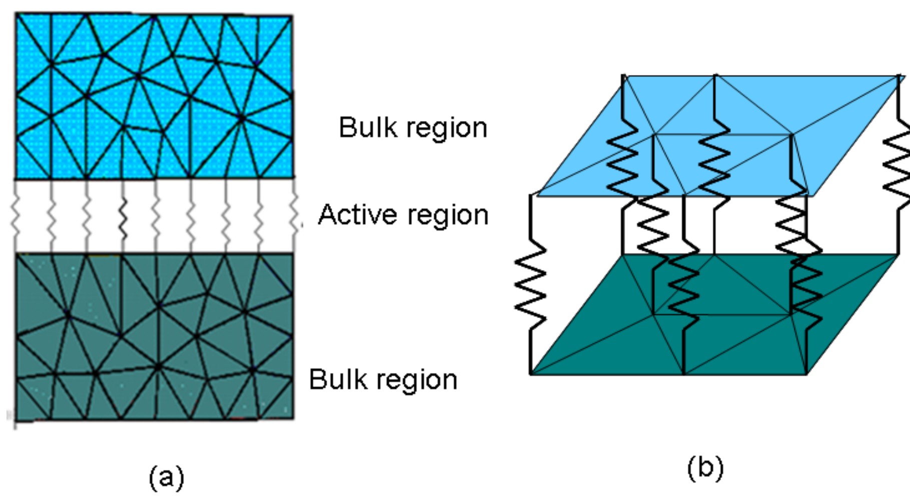

Figure 7: Depiction of the Active resistor model : (a) Cross sectional view (b) 3D view

CHAPTER II

FORMULATION AND IMPLEMENTATION

2.1 Physical model

The physical model used for simulating the 3D current flow in bulk regions is based on the hybrid 3D/1D model described in the previous section. The effective application of this model for the LED [20] provides the inspiration for its usage in the 3D simulation of Photonic crystal VCSELs. The adaptation of this model for the physics involved in the laser and most of the modeling and implementation of the physical phenomena in the active layer was done by Dr. Alexey Maslov from Canon USA. The current continuity equation is used to model the bulk regions, and the active (gain) region of the laser is modeled in 1D using one of multiple models that vary in complexity.The simplistic active resistor 1D model, used for the simulation documented in this thesis, is described; however, a more sophisticated drift-diffusion model is being implemented. The 1D model also includes solving the photon rate equation to obtain the light intensity. The optical mode pattern is calculated independently of this simulation and can be obtained using any optical solver. An optical solver based on the transfer matrix method is used for the simulations in this thesis. This solver was developed by Dr Frank Cao at Canon USA.

2.1.1 Current Continuity

The bulk regions of the device exhibit a linear relationship between the drift current density and the potential in the device. In case of the VCSEL structure, the bulk regions consist primarily of the substrate and the DBR layers. The linear relationship is given by the current continuity equation.

$$\nabla.\vec{J} = -\frac{\partial \rho}{\partial t} \quad (1)$$

Non equilibrium recombination and generation of carriers in the bulk regions of the device in neglected for now, due to low minority carrier densities. It is assumed that the bulk region of the device has a constant steady state charge density. The right hand side of the above equation can then be assumed to be zero.

Using $\vec{J} = \sigma\vec{E}$ and $\vec{E} = -\nabla\phi$ we have $\nabla.\{\sigma\nabla\phi\} = 0$ (2)

Here $\vec{E}$ is the electric field vector and ϕ is the electrostatic potential. Equation (2) is then discretised using the box integration technique in 3D. This differential equation uses two types of boundary conditions:

1) Dirichlet boundary conditions for the electrodes, $\phi_{electrode} = Applied\ potential$. The potential at every node on the electrode is the voltage applied to the electrode. Usually one of the electrode is fixed at 0V and the other electrode's voltage is the potential difference between the two electrodes.

2) Neumann boundary conditions at the non - electrode device boundaries $\frac{\partial \phi}{\partial n} = 0$. Since there is no current flowing out of the device, the normal derivative of potential at all non electrode surface points should be zero.

2.1.1.1 Discretization of the Continuity equation

The discretization of the continuity equation is done on a tetrahedral 3D grid. The box integration technique is used for the discretisation. The box integral technique applies the continuity equation to every volumetric cell in 3D. These volumetric cells are constructed such that they encompass the whole volume of the device, and every discretised node has a volumetric unit associated with it such that every point in that volume is closer to that node than any other node. Such volumetric cells are called

'Voronoi volumes'.The 2D equivalent of a Voronoi volume is a Voronoi area. A 2D mesh and the corresponding Voronoi areas are depicted here.

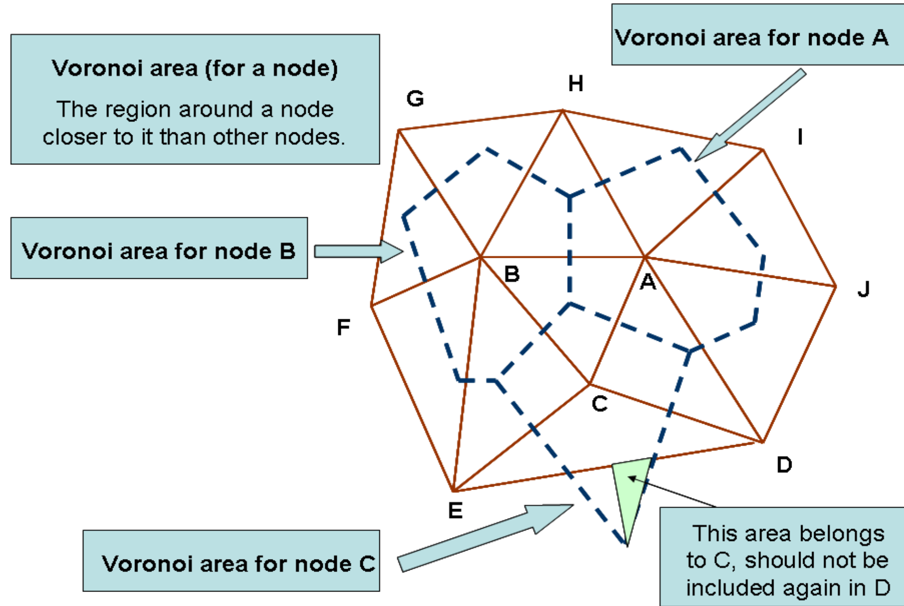

Figure 8: 2D mesh and voronoi areas for the nodes

As shown in the above figure, the voronoi areas for a node in 2D are formed by the intersection of the perpendicular bisectors of the lines joining the node to neighbouring nodes. Similarly in 3D, the Voronoi volumes are formed by the intersection of the bisecting planes for each line. Since the discretisation is not guaranteed to be conforming Delaunay in 3D,we have to work with constrained Delaunay meshes. In this case, careful calculation of the Voronoi areas is required in the presence of obtuse angled triangles or tetrahedra. This is because a part of the Voronoi area for the node can extend beyond the triangles to which the node belongs. Each Voronoi area or volume is unique to a node and there should not be overlapping Voronoi areas or volumes. Hence, if the above method for calculating Voronoi areas leads to overlapping Voronoi areas, the overlapping area should be included in the Voronoi area of only a single node.

The current continuity equation is discretised by applying a box integration on

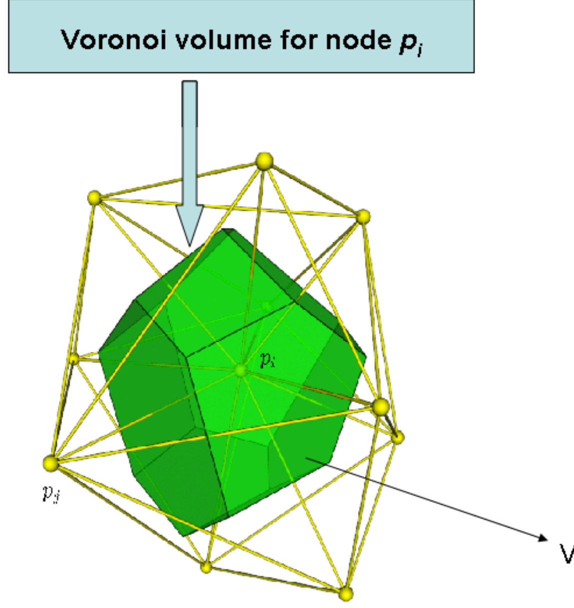

Figure 9: Depiction of 3D Voronoi volume for node i.[2]

the Voronoi volume.The technique used here is similar to the one followed in the discretisation of the Poisson equation[5].

$$\int_V \nabla.\left(\sigma\nabla\phi\right)\partial v = 0 \tag{3}$$

Using the divergence theorem, the above integral can be converted to a surface integral

$$\oint_{\partial V} \left(\sigma\nabla\phi\right)\cdot \mathbf{dA} = 0 \tag{4}$$

This surface integral for the Voronoi box of a node can then be approximated as a summation over all the partial areas that make up the Voronoi box for that node. Here, we assume that the component of the gradient normal to each partial area is constant over that partial area. These partial areas are present in various tetrahedra to which the node belongs. In case of region boundaries, the tetrahedra connecting

to a node might lie in different regions and can have different properties, in this case σ. Hence it is advantageous to deal with the surface integral by accumulating partial sums in all tetrahedra. Currently, no special treatment is given to tetrahedra on the having boundary facing obtuse angles at region interfaces, as the occurrence of such cases is rare. The Voronoi box for such a point might extend into the other region and hence might have to be dealt with carefully for more accurate modelling. The gradient of the potential is also approximated using finite differences and this leads to the discrete form of the equation.

$$\sum_{tet_i, \forall p_i p_j} \sigma_i \frac{\phi_n - \phi_m}{d_{mn}} A_{t_i} = 0 \tag{5}$$

This equation is for a single node. Here the summation is performed for all the edges connected to that node in all the tetrahedra to which the node belongs.ϕ_m, ϕ_n are the potentials at nodes m and n.For a given node, one of the nodes is fixed and all the other nodes connected to it contribute to the equation. The partial area A_{t_i} in a tetrahedron is a contribution to the total surface area of the Voronoi box. Within any tetrahedron, for a given edge $p_i p_j$, the partial area is the quadrilateral formed by the circumcenters of the two triangles to which the edge $p_i p_j$ belongs, the midpoint of $p_i p_j$ and the circumcenter of the circumsphere for the whole tetrahedron. These points and the calculation for the partial area are depicted in the Figure 10.

In the presence of obtuse angles, the simple summation of triangle areas might lead to erroneous partial areas as depicted in Figure 8. This is avoided by calculating signed areas for the triangles. The order of the points in a tetrahedron is fixed and the areas are calculated by cross products which result in positive or negative areas. This calculation accounts for the orientation of the circumcenters with respect to the nodes and the midpoints, and hence calculates the appropriate partial area in that tetrahedron. Note that the partial area for an edge in one tetrahedron can be negative, but the total partial area associated with an edge should be positive. This

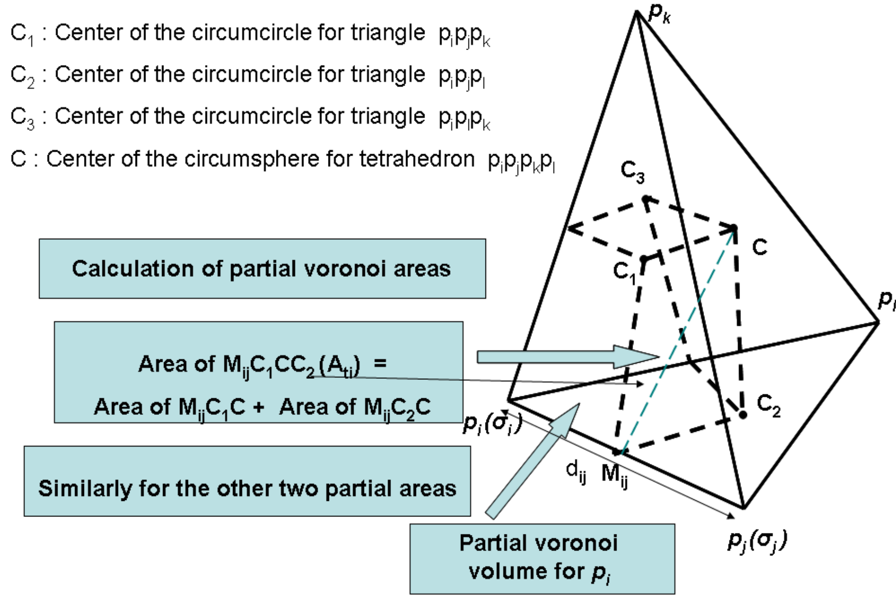

Figure 10: Calculation of partial areas of the Voronoi box

is automatically ensured if the mesh is constrained Delaunay.

2.1.2 Active region model

The continuity equation in the bulk region is coupled to the active region model through the points on the top and bottom of the active layer. This is essentially boundary matching at the interfaces of the layers. The active region can be modeled with varying complexity depending on the desired speed and accuracy of the simulation. The model used in the simulations is discussed below and a brief overview of a few other models under development are provided.

2.1.2.1 Effective resistor model

A two dimensional plane coincides with the location of the active region in the device in our 3D tetrahedral mesh. The nodes on the plane representing the active region are duplicated to obtain their counterparts on the other side of the active region. We assume that the current spreading is minimal in the thin active region, so that each point on the active region plane is only coupled to its lower counterpart. In this way,

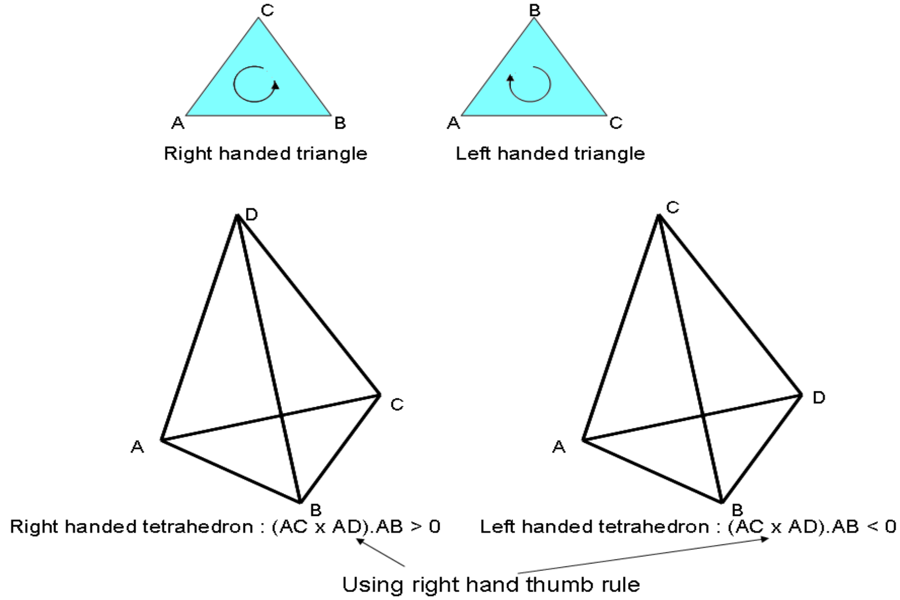

Figure 11: Orientations of triangles and tetrahedra

the active region modeling is reduced to a set of parallel 1D equations. These should be solved consistently with the bulk region continuity equations. The problem is still non linear, but the non-linearity is reduced significantly and restricted to the active region. This approximation may be lifted later to solve for current spreading in the active region.

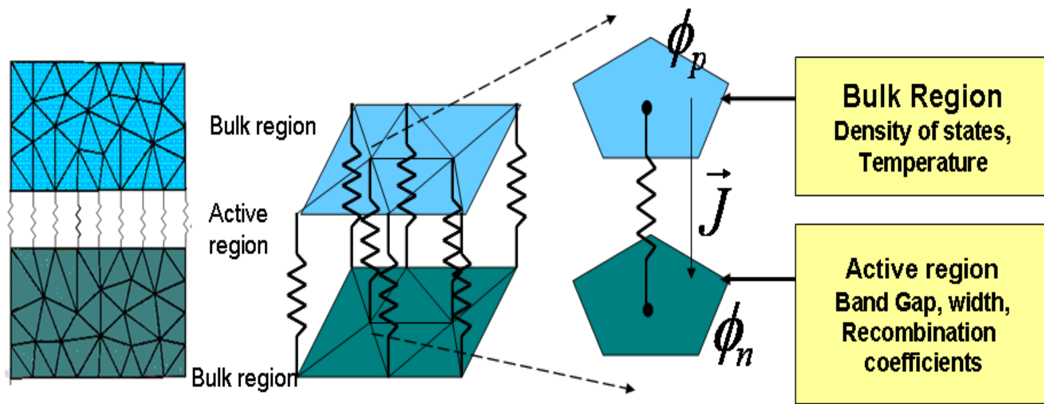

Figure 12: Active resistor Physical model

The resistors indicated in Figure 12 represent the 1D coupling between a point on

the top of the active layer and a point on the bottom. Each of the resistors represents a relation between the current flow through the active region and the potential drop across the active region for that resistor (2D region). The charge carriers in the QW active region must satisfy the carrier balance equation. Here we assume that the electron and hole concentrations are equal. Finally the current density obtained from the potential drop in the active region should satisfy the continuity equation in the adjacent bulk regions. These conditions are represented mathematically below.

$$\mu_c + \mu_v + E_g - qU = 0 \tag{6}$$

Equation 6 relates the external potential drop to the electrochemical potentials at the active region boundaries. μ_c and μ_v are the electrochemical potentials on the n and p sides of the junction region, E_g is the band gap of the device and U is the electrostatic potential drop. The electro chemical potentials are related to the carrier concentrations by the following equations. The linear resistance of the active region is neglected in this equation.

$$\frac{\mu}{kT} = \ln\left(\frac{N}{N_{eff}}\right) + K_1 \ln\left(\frac{K_2 N}{N_{eff}} + 1\right) + \frac{K_3 N}{N_{eff}} \tag{7}$$

where N is the carrier concentration in the quantum well, and N_{eff} is the effective density of states in the quantum well, and K_1, K_2 and K_3 are constants. Equation 7 provides a good approximation to the Fermi-Dirac Integral for parabolic bands. [27]. Using Equation 7 and Equation 6, we can solve for the carrier concentration for a given U using a non-linear iterative technique.

The current density across this resistor is then calculated using the carrier balance equation. In steady state, assuming unity internal efficiency,

$$\frac{dN_w}{dt} = \frac{J_{in}}{q} - R_{st} - R_{sp} - R_{nr} = 0 \tag{8}$$

where R_{st} is the stimulated recombination, R_{sp} is the spontaneous recombination term, R_{nr} is the non radiative recombination term (thermal and Auger recombination)and J is the vertical current density for a given area in the active region(representing one active resistor). N_w = Nd is the 2D carrier density for a quantum well of width d. The recombination terms are related to the carrier density by the following equations

$$R_{st} = \gamma G_w N_{ph} \qquad R_{sp} = dBN^2 \qquad R_{nr} = d\left(AN + CN^3\right) \tag{9}$$

where G_w is the carrier density dependent gain per unit area,N_{ph} is the number of photons in the cavity, and γ is the confinement factor per unit volume or the fraction of the light energy in the quantum well (active region). B is the spontaneous recombination coefficient, A is the coefficient for band to bound recombination due to defect states and C is the Auger recombination coefficient. The current density calculated in this manner acts as a boundary condition to the continuity equation in the bulk regions and should equal the current density leaving the p side of the active region interface and entering the n side. Finally we also have the optical part of the problem for which the photon rate equation is solved

$$\frac{dN_{ph}}{dt} = -\frac{N_{ph}}{\tau_c} + \mathcal{G}N_{ph} + R_{sp} \tag{10}$$

where τ_c is the photon lifetime. The confinement factor and the photon lifetime are dependent on the optical modes of the laser. These are obtained from an optical solver.

2.1.2.2 Discretisation of the effective resistor model

As it was shown in the previous section, the active resistor model for a 3D simulation is used by dividing the thin active layer simulation region into a set of 1D resistors.Essentially, the model is applied to the 1D active resistors with the potential

difference across the resistor as the input. The output is the current density and carrier density for each resistor. Each effective resistor acts as a lumped model for the processes in the active region which were defined in the previous section. Hence, the effective discretisation for the effective resistor model happens only in the 2D plane. After the carrier concentration is obtained for each effective resistor, Equation 6 is applied for each resistor. Hence, the number of points on the 2D plane or the number of active resistors is equal to the number of active layer equations that have to be self consistently solved with the bulk continuity and the photon rate equations.

2.1.2.3 Example formulation for the effective resistor model

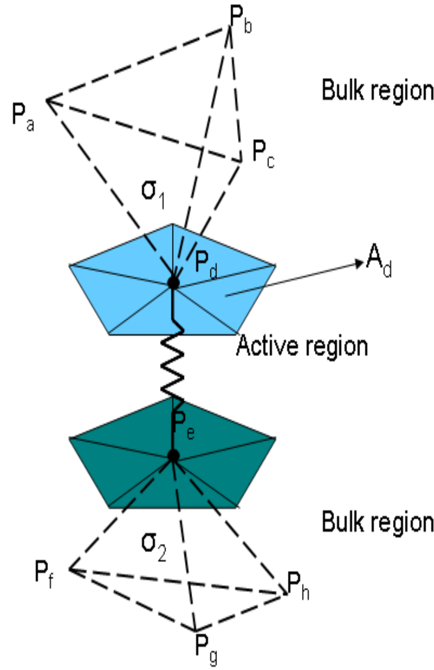

Figure 13: Active resistor formulation

The above figure shows an active resistor and a tetrahedron connected to each end of the active resistor. The potential at each point P_n is denoted by ϕ_n. The potential at each point, together with the photon number N_{ph} form the unknowns in the device.

Consider the points P_d and P_e on the two sides of the active layer.These points denote an active resistor. They are co-located in the 3d model of the surrounding bulk regions. This active resistor models the whole voronoi area A_d surrounding P_d and P_e. The continuity equations at point P_d and P_e can be written as

$$-\frac{(\phi_a - \phi_d)}{d_{ad}}\sigma_1 A_{ad} - \frac{(\phi_c - \phi_d)}{d_{cd}}\sigma_1 A_{cd} - \frac{(\phi_b - \phi_d)}{d_{bd}}\sigma_1 A_{bd} + A_d J(\phi_d - \phi_e, N_{ph}) = 0 \quad (11)$$

$$-A_d J(\phi_d - \phi_e, N_{ph}) + \frac{(\phi_f - \phi_e)}{d_{fe}}\sigma_2 A_{fe} + \frac{(\phi_g - \phi_e)}{d_{ge}}\sigma_2 A_{ge} + \frac{(\phi_h - \phi_e)}{d_{he}}\sigma_2 A_{he} = 0 \quad (12)$$

d_{ij} is the distance between the points P_i and P_j

A_{ij} is the partial area perpendicular to the edge P_iP_j

σ_1 and σ_2 are the conductivities of the bulk regions

Each of the terms in the equations represent current. Since the current continuity is applied to a node, the current flowing into the node is considered negative and current flowing out of the node is considered positive. $J(\phi_d - \phi_e, N_{ph})$ is the current density in the active resistor. It should be noted that J is a non linear function of the potential difference and the current entering node P_e is also denoted as $J(\phi_d - \phi_e, N_{ph})$ and not $J(\phi_e - \phi_d, N_{ph})$. The current leaving the node P_d of the active resistor is the same as that entering the node P_e.

2.1.2.4 Photon rate equation

The optical properties of any laser's gain medium can be treated using the photon rate equation.

$$\frac{dN_{ph}}{dt} = -\frac{N_{ph}}{\tau_c} + \mathcal{G}N_{ph} + R_{sp} \quad (13)$$

The photon rate equation can be derived from Maxwell's equations using classical techniques [44] or using the quantum hypotheses and Einstein's A and B coefficients

[61]. The first term on the right hand side of the equation represents cavity losses via photon absorption or escape processes. τ_c is the photon lifetime in the cavity and is provided by the optical solver. The term $\mathcal{G}N_{ph}$ represents the rate of change in photon number due to stimulated emission. $\mathcal{G}$ represents the modal gain coefficient in the cavity. This depends on the carrier density dependent material gain G_w by the following relationship.

$$\mathcal{G} = \iint \gamma(x, y) G_w(x, y) dxdy \tag{14}$$

where $\gamma(r)$ is the confinement factor for the optical modes in the cavity and the integration is performed over the entire active region. This is obtained from an optical solver based on the geometry and material properties of the device. In our case, the 2D plane is discretised into a set of active resistors and the above integral has to be approximated to a summation over all optical resistors.

$$\mathcal{G} = \sum_{active\ resistor\ R_i} \gamma_i G_{w_i} \tag{15}$$

In the classical form, the gain G_w is expressed in terms of the susceptibility and permittivity of the device as

$$G_w = -\,\omega_0 \frac{4\pi\chi^{''}}{\epsilon^{'}} \tag{16}$$

where $\chi^{''}$ is susceptibility of the quantum well and $\epsilon^{'}$ is the permittivity of the gain region.

However, in the implementation of this model, the susceptibility is not used and G_w is calculated using a linear approximation involving the carrier density N, the differential gain D and the transparency density.

$$G_w = D(N - N^{tr})d \tag{17}$$

where d is the width of the recombination region.

The last term in the photon rate equation denotes the spontaneous emission term. Note that this term is independent of the number of photons in the cavity, but is proportional to the number of carriers in the active region which recombine spontaneously to emit a photon. The proportionality constant β can be a function of the position and hence the spontaneous emission term can be given as

$$R_{sp} = \iint \beta R_{sp}(x, y) dx dy \tag{18}$$

The implementation, however, approximates the proportionality factor to a constant term and uses the active resistor discretisation to reduce the above equation to a summation

$$R_{sp} = \sum_{active\ resistor\ R_i} \beta R_{sp_i} \tag{19}$$

R_{sp_i} is a function of N and implicitly a function of potential difference U. Hence the active resistor model supplies the Gain G_w, the Current density J, and the spontaneous emission term R_{sp}, given the potential difference U, and the number of photons N_{ph}.

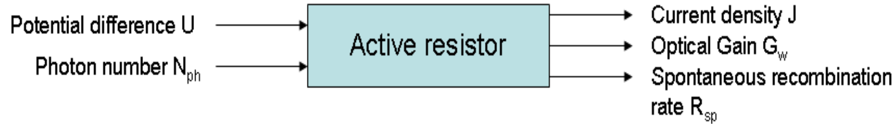

Figure 14: Active resistor functionality

2.2 *Coupling and Newton's method*

The non linear active region, the bulk regions which obey a linear current continuity relation and the photon rate equation are coupled together to find the potentials and photon number in the device self consistently. The non linearity and the coupling

between various terms require the use of an iterative method to obtain the self-consistent solutions for the equations. Newton's method with adaptive iteration step size is used for this purpose. The active resistor model provides the carrier density, gain and spontaneous emission for a given potential difference and photon number. These are used as part of the Jacobian, to obtain the solution variables, which are the potentials and the photon number at each node. If the total number of nodes are N and the number of active resistors are R, we have N + 1 equations of which R + 1 equations are non-linear (photon rate equation included) and N - R linear equations which deal with the bulk nodes.

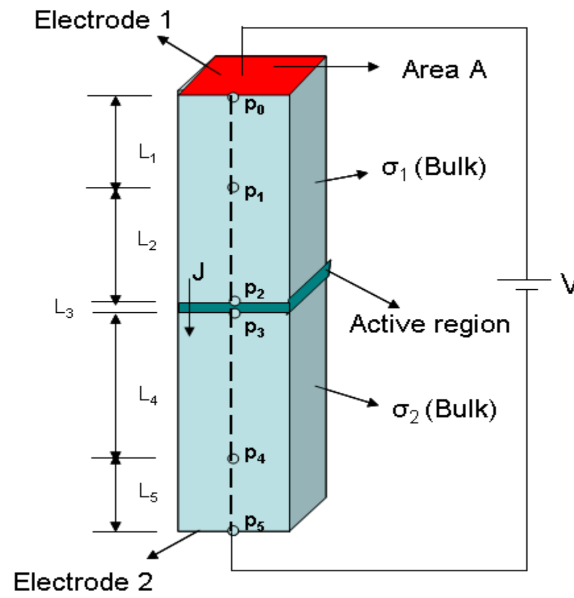

Figure 15: 1D formulation for the active resistor model

Let us consider the formulation of the matrix in one dimension. Figure 15 shows a simple laser diode with the bulk regions, active regions and electrodes specified. For the purpose of explaining the numerical method, only one dimension is discretised. The points $p_0, p_1, p_2, p_3, p_4, p_5$ are the discretised points. The lengths between these points are denoted by $L_0, L_1, L_2, L_3, L_4, L_5$. A potential V is applied to the electrodes.

Hence the boundary points p_0 and p_5 will have Dirichlet boundary conditions.The unknowns in this case are the potentials at the discretised nodes $\phi_0, \phi_1, \phi_2, \phi_3, \phi_4, \phi_5$ and the photon number N_{ph}. The set of equations that model the device in 1D can be written as

$$\phi_0 = V \tag{20}$$

$$-\frac{(\phi_0 - \phi_1)}{L_1} A\sigma_1 + \frac{(\phi_1 - \phi_2)}{L_2} A\sigma_1 = 0 \tag{21}$$

$$-\frac{(\phi_1 - \phi_2)}{L_2} A\sigma_1 + AJ((\phi_2 - \phi_3), N_{ph}) = 0 \tag{22}$$

$$-AJ((\phi_2 - \phi_3), N_{ph}) + \frac{(\phi_3 - \phi_4)}{L_4} A\sigma_2 = 0 \tag{23}$$

$$-\frac{(\phi_3 - \phi_4)}{L_4} A\sigma_2 + \frac{(\phi_4 - \phi_5)}{L_5} A\sigma_2 = 0 \tag{24}$$

$$\phi_5 = 0 \tag{25}$$

$$-\frac{N_{ph}}{\tau_c} + A\gamma G_w N_{ph} + A\beta R_{sp} = 0 \tag{26}$$

where $J((\phi_2 - \phi_3), N_{ph})$ is the current density in the active region.

2.2.1 Newton's method

In the above set of equations, Equations 22, 23 and 26 are non linear, since each of the functions $J((\phi_2 - \phi_3), N_{ph})$, $G_w((\phi_2 - \phi_3), N_{ph})$ and $R_{sp}((\phi_2 - \phi_3), N_{ph})$ are non linear. Hence the set of equations cannot be solved using direct matrix methods. Newton's method uses the following approach to the non linear equations.

Let us denote the set of equations obtained above $f(\phi_0, \phi_1, ..\phi_5, N_{ph})$ as

$$f_0(\phi_0, \phi_1, ..\phi_5, N_{ph}) = 0$$
$$f_1(\phi_0, \phi_1, ..\phi_5, N_{ph}) = 0$$
$$\vdots$$
$$f_6(\phi_0, \phi_1, ..\phi_5, N_{ph}) = 0$$

and the set of unknowns as $S = [\phi_0, \phi_1, \cdots, N_{ph}]$. To solve this set of equations we start with an initial guess for the entire solution $S^0 = \left[\phi_0^0, \phi_1^0, \cdots, N_{ph}^0\right]$. Since this is not the solution to the equation (unless we are very lucky!), the value of $f(\phi_0, \phi_1, ..\phi_5, N_{ph})$ at S^0 will not be zero. We note this residual called $f(S^0)$ and seek to find a better guess for S based on this residual. To do this, we use a linear function that passes through $f(S^0)$ and is tangential to $f(S)$. Such a function is represented by the slope of $f(S)$ at S^0 and is denoted by $f^{'}(S^0)$, which is called the Jacobian matrix. Then we can write an equation for the linear function as

$$f(S^0) = f^{'}(S^0)(S^0 - S^1) \tag{27}$$

where S^1 is the set of values where the linear function equals zero.S^1 can be computed from Equation 27 using direct matrix methods. This requires that all the other quantities $S^0, f(S^0)$ and $f^{'}(S^0)$ are known. If this is true, then S^1 is the new guess for the solution set. If the initial guess is appropriately made, then multiple iterations of the above technique will converge to the solution. In general

$$f(S^i) = f^{'}(S^i)(S^i - S^{i+1}) \tag{28}$$

$$S^{i+1} = S^i - f^{'}(S^i)^{-1} f(S^i) \tag{29}$$

A solution is obtained when the residual $f(S^i)$ is below a determined threshold. It is important to note that the inverse operation of $f^{'}(S^i)$ is $f^{'}(S^i)^{-1}$, since the variables are arrays and this is a matrix operation.

2.2.1.1 Convergence of Newton's method

The method described above is not guaranteed to converge to the solution after repeated iterations. Although this is a good technique to solve non-linear equations, one must take into account the conditions required for the technique to converge.

The first condition is the availability of all the terms in Equation 29 to calculate S^{i+1}. Since S^i is known and we know the set of equations $f(S)$, we also know $f(S^i)$. Hence we need to ensure that the term $f^{'}(S^i)$ can be determined. Also if $f^{'}(S^i) = 0$, its inverse does not exist, the guess is not updated and there is no possibility for convergence. For example, in the one-dimensional case if $f(x) = 1 + x^2 - 2x$ and if the guess $x^0 = 0$, we have $f^{'}(x^0) = 0$ and hence x^1 cannot be determined, although the actual solution $x = 1$ is close enough.

To check if $f^{'}(S)$ can be determined in the 1D modeling for the laser diode, we need to find the derivatives of each nodal equation with respect to each independent variable. An approximation of the derivatives using differences in end points leads to the secant method which is not as effective as the Newton's method. The matrix $f^{'}(S)$ or the Jacobian of $f(S)$ can be written as

$$A_{ij} = \frac{\partial f_i}{\partial S} = \begin{bmatrix} 1 & 0 & 0 & 0 & 0 & 0 & 0 \\ A_{10} & A_{11} & A_{12} & 0 & 0 & 0 & 0 \\ 0 & A_{21} & A_{22} & A_{23} & 0 & 0 & A_{26} \\ 0 & 0 & A_{32} & A_{33} & A_{34} & 0 & A_{36} \\ 0 & 0 & 0 & A_{43} & A_{44} & A_{45} & 0 \\ 0 & 0 & 0 & 0 & 1 & 0 & 0 \\ 0 & 0 & A_{62} & A_{63} & 0 & 0 & A_{66} \end{bmatrix} \tag{30}$$

where the non zero Jacobian terms are given by

$$
\begin{array}{llll}
A_{10} = -A\dfrac{\sigma_1}{L_1} & A_{11} = A\left(\dfrac{\sigma_1}{L_1} + \dfrac{\sigma_1}{L_2}\right) & A_{12} = -A\dfrac{\sigma_2}{L_2} & \\
A_{21} = -A\dfrac{\sigma_1}{L_2} & A_{22} = A\dfrac{\sigma_1}{L_2} + A\dfrac{\partial J}{\partial U} & A_{23} = -A\dfrac{\partial J}{\partial U} & A_{26} = A\dfrac{\partial J}{\partial N_{ph}} \\
A_{32} = -A\dfrac{\partial J}{\partial U} & A_{33} = A\dfrac{\sigma_2}{L_4} + A\dfrac{\partial J}{\partial U} & A_{34} = -A\dfrac{\sigma_2}{L_4} & A_{36} = -A\dfrac{\partial J}{\partial N_{ph}} \\
A_{43} = -A\dfrac{\sigma_2}{L_4} & A_{44} = A\left(\dfrac{\sigma_2}{L_4} + \dfrac{\sigma_2}{L_5}\right) & A_{45} = -A\dfrac{\sigma_2}{L_5} & \\
A_{62} = A\gamma\dfrac{\partial G_w}{\partial U}N_{ph} & A_{63} = -A_{62} & \multicolumn{2}{l}{A_{66} = -\dfrac{1}{\tau_c} + A\gamma G_w + A\gamma N_{ph}\dfrac{\partial G_w}{\partial N_{ph}} + A\beta\dfrac{\partial R_{sp}}{\partial N_{ph}}}
\end{array}
$$

The partial derivatives mentioned in the above formulae are listed below. Since these can be calculated analytically, we can conclude that the Jacobian can be determined. Nevertheless, we cannot conclude if the Jacobian is singular because this depends on the guess made for the unknowns and the updates obtained in further iterations.

$$
\frac{\partial J}{\partial U} = q\left(\gamma N_{ph}DL_3 + 2BNL_3 + AL_3 + 3CN^2L_3\right)\frac{\partial N}{\partial U} \qquad \frac{\partial J}{\partial N_{ph}} = g\gamma G_w \tag{31}
$$

$$
\frac{\partial G_w}{\partial U} = D\frac{\partial N}{\partial U}L_3 \qquad \frac{\partial G_w}{\partial N_{ph}} = 0 \tag{32}
$$

$$
\frac{\partial R_{sp}}{\partial U} = 2BN\frac{\partial N}{\partial U}L_3 \qquad \frac{\partial R_{sp}}{\partial N_{ph}} = 0 \tag{33}
$$

In addition to the availability of the Jacobian, convergence to the solution also depends on the initial guess and the nature of the function. An inappropriate initial guess might lead to an oscillatory pattern in the Newton iteration. This is illustrated in the one dimensional example of Newton's method, where the same initial guess is used for two different functions. In such an event, a different initial guess can be chosen and the iteration can be repeated.

The simulation analysis of the device is done by calculating the potential and current density distribution for various applied external voltages. In this case, the

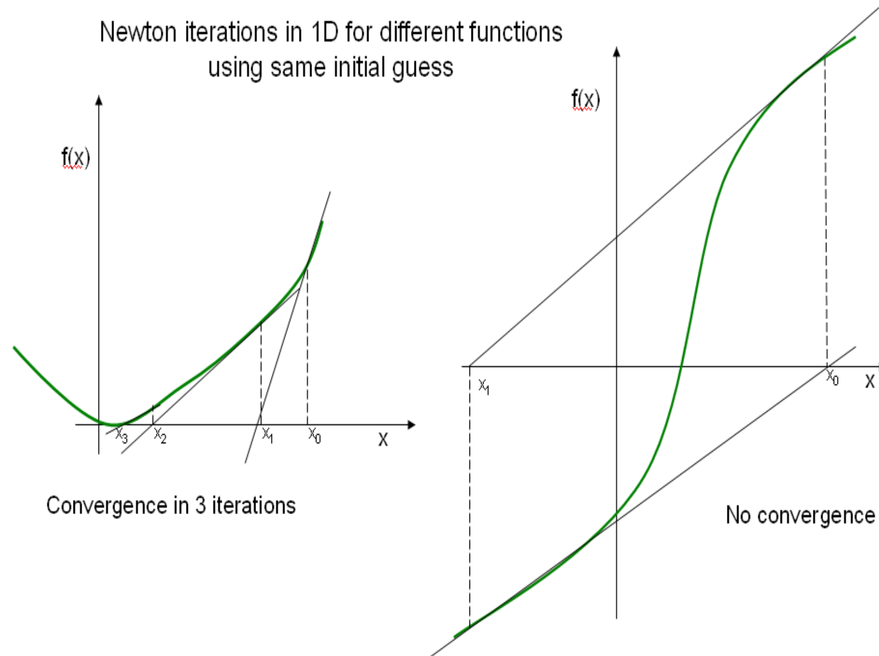

Figure 16: Convergence of Newton's method in 1D

initial guess for every external voltage is the solution obtained for the previous voltage. Since the device characteristics do not change abruptly, this leads to initial guesses in the vicinity of the solution, as a result of which there is fast convergence. If convergence is not obtained at a particular voltage, the previous guess is considered to be too far and an intermediate voltage step is used to obtain a better guess. If the device behaviour is to be modeled at a single higher voltage, it is still advisable to find solutions at lower voltages, albeit, at large voltage steps, increasing the likelihood of convergence.

Convergence is determined by the magnitude of the function $f(S)$. Since the functions describe different variables with different magnitudes, the threshold for each type of function needs to be different. In the implementation, a combination of absolute and relative errors are used to determine the threshold for convergence. The three different types of equations in the formulation are

a) Dirichlet boundary conditions (potential V)

b) Current continuity equations (current A)

c) Photon rate equation (Number of photons/sec)

The criterion for convergence of any function $f_i(S)$ is given by

$$|f_i(S)| \leq \epsilon_a + \epsilon_r \sum_{alltermsj} \left| f_i^j(S) \right| \tag{34}$$

where ϵ_a is the absolute error and varies for the three types of equations, while ϵ_r is the relative error, which is the same for each type of equation.

2.3 Implementation and algorithms

The simulator has been developed in the C programming language. The simulation involves calculating the geometrical properties of the discretised structure, reading in the device properties, setting up the equations for the bulk and active regions, coupling these equations and solving these equations using the Newton's method. The active resistor model is used as a library in the simulation. This modularity allows us to replace the description of the active layer with another model, provided the interface is defined correctly. The algorithms performing these tasks are captured in the flowcharts provided below.

2.3.1 Bulk transport and coupling to active region and cavity

The master function for the simulator is the threedeesim() routine. This routine is described in the flowchart below. The decisions that are made based on the input file parameters are provided. The coupling of the active region to the optical cavity can be controlled by the user. In the case where the active region is coupled to the cavity,the simulator requires the presence of confinement factors for the device. If these are not available, the simulator exits and provides the geometry of the device, so that an external optical solver can be used to find the confinement factors.

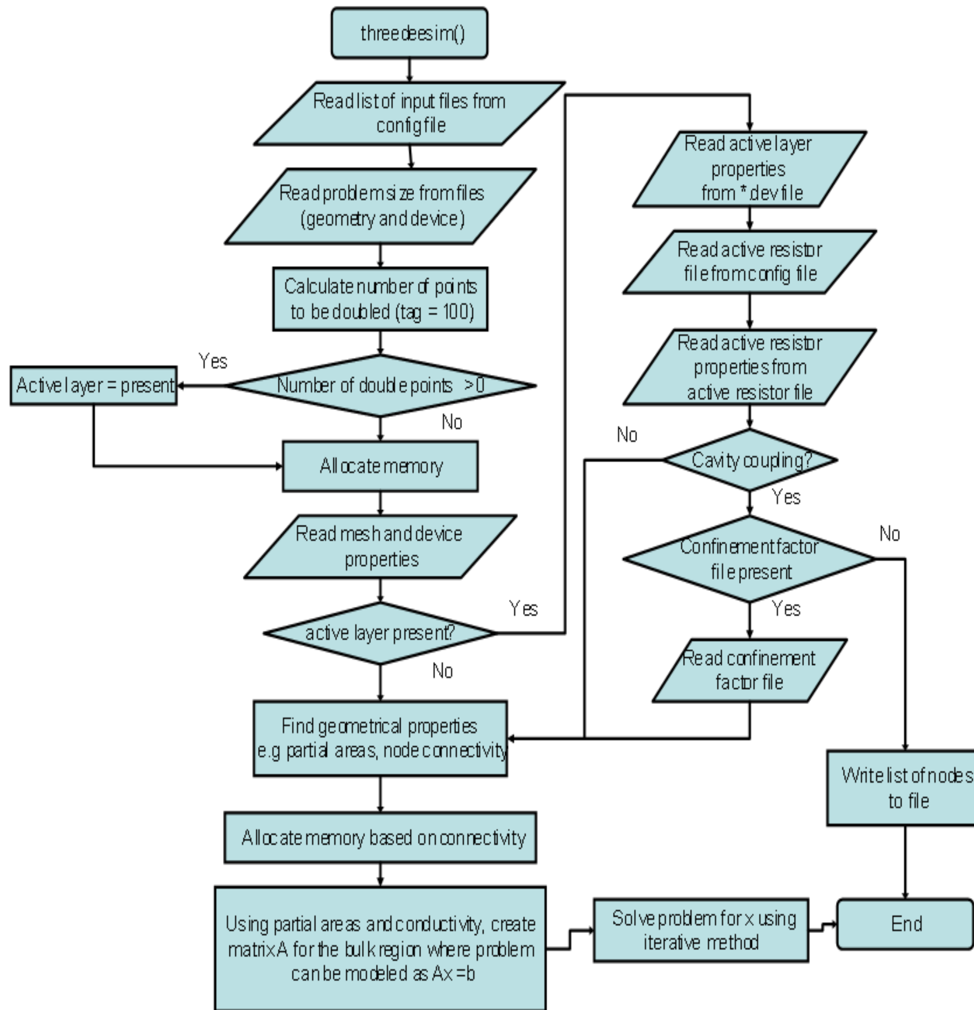

Figure 17: Top level flowchart for the simulator

2.3.2 Voltage stepping and iterative solutions

The laser characteristics are obtained by voltage stepping from a value below the lasing threshold to voltage values above the threshold. A moderate voltage stepping is sufficient to achieve convergence above and below threshold, but at voltages near to lasing threshold, convergence is difficult to achieve unless the electrode potentials are varied in small steps. This is captured in the flowchart shown in Figure 18.

The implementation of the Newton's method and the steps involved in calculating the Jacobian and the right hand sides of the $f(S)$ system of equations are described below.

2.3.3 Active resistor model

The active resistor library calculates current density, gain and spontaneous emission term for every iteration in the Newton's method. Every iteration passes a new value for the potential drop across the active resistor and the number of photons in the cavity and calls the active_resistor_update function to calculate the new current density, gain and spontaneous emission terms. This is indicated in the flowchart below. The active layer library also has an option to treat the current flow in the active region as a linear function of potential.

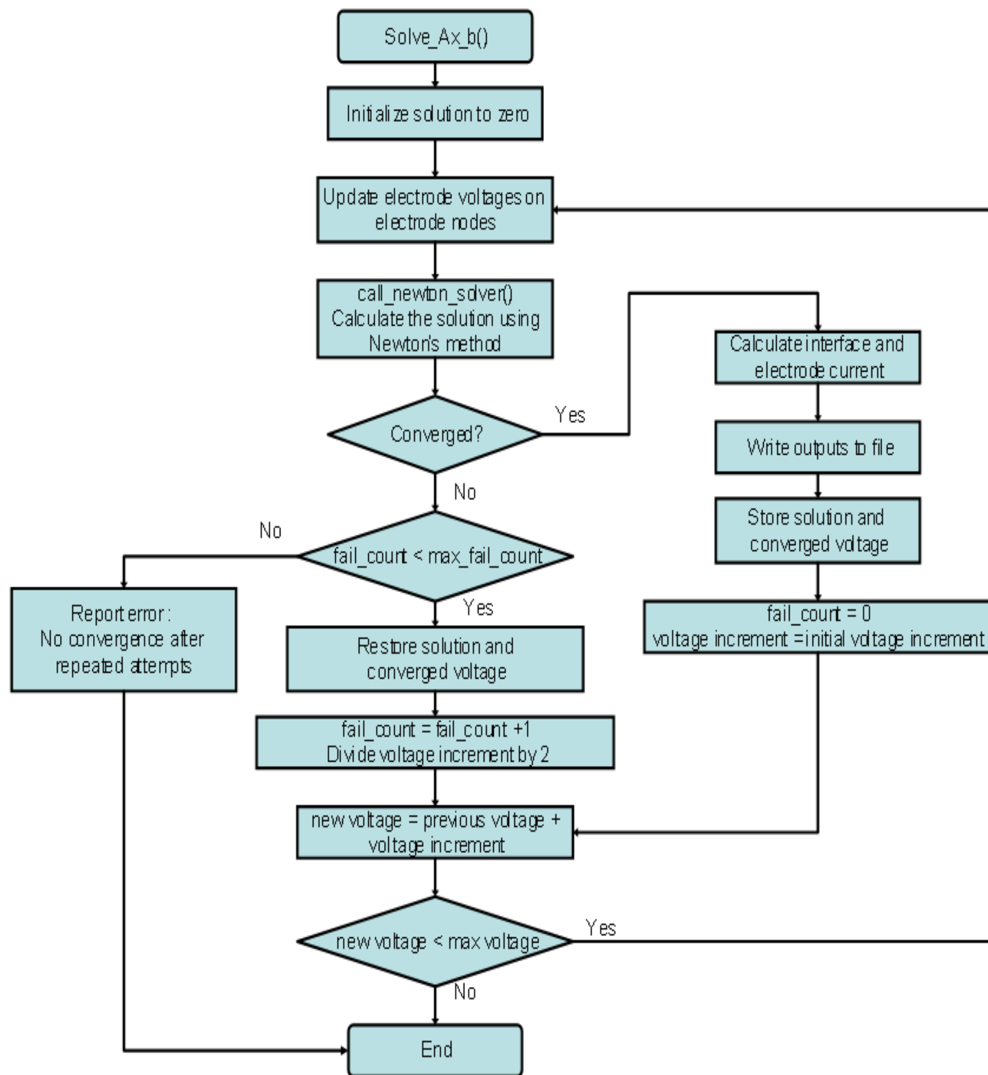

Figure 18: Flowchart for voltage loop and convergence handling

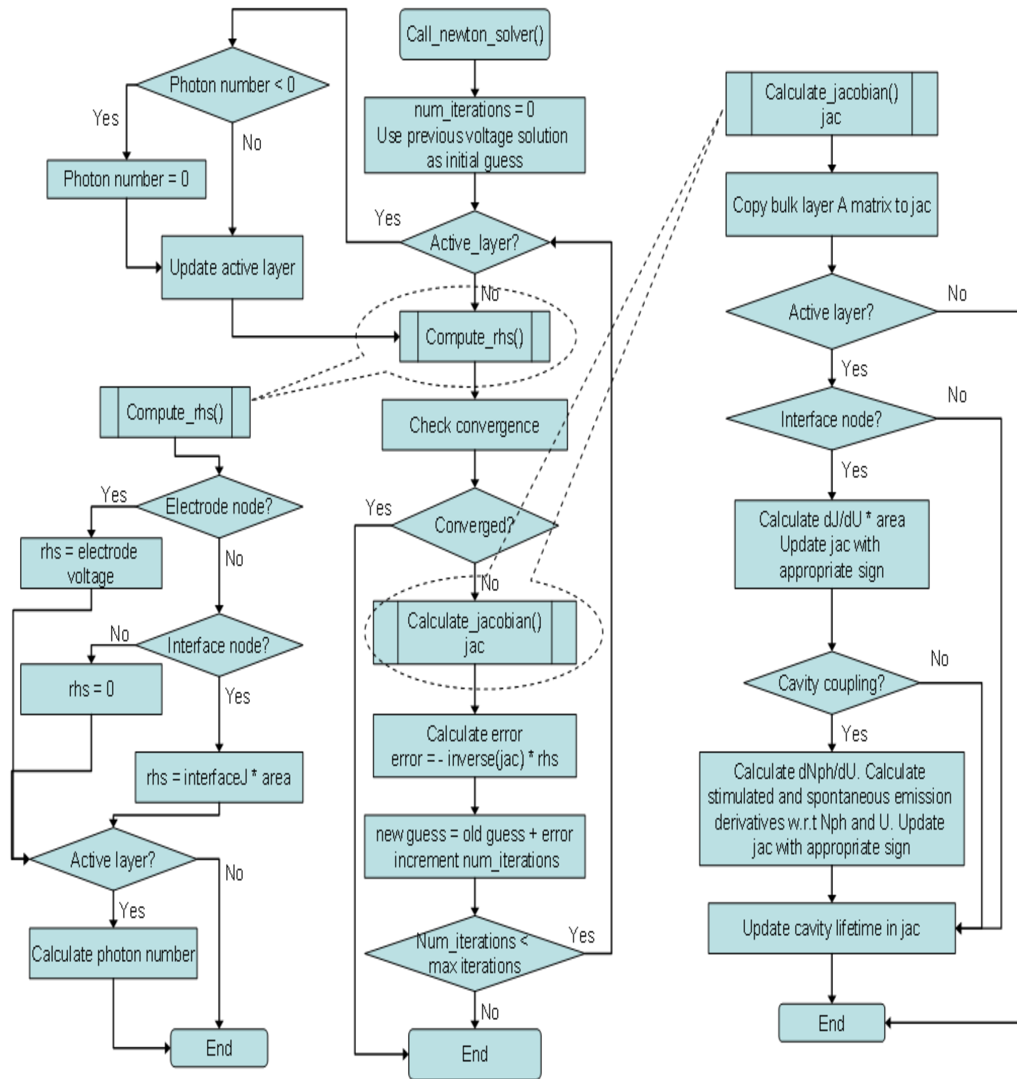

Figure 19: Program flow for the Newton's method

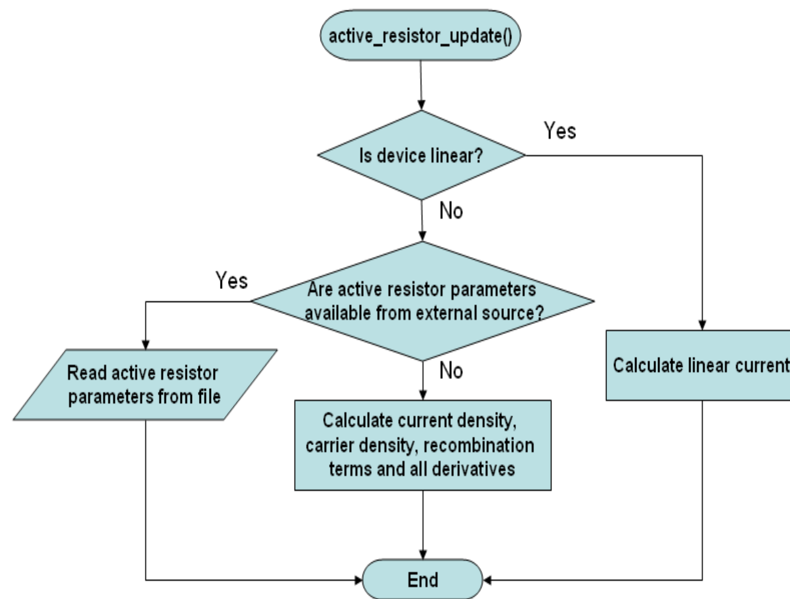

Figure 20: Flowchart for active resistor update

CHAPTER III

RESULTS

The 3D simulator provides a fast and efficient method of obtaining the current and light intensity characteristics of many laser structures. The validation of different parts of the simulator has also been performed, and these results are provided in this section. A comparison is also made with some experimental results for a basic VCSEL structure. Performance issues such as speed and discretisation accuracy are provided.

3.1 Validation of continuity equation

The continuity equation is used for all the nodes in the bulk regions. The formulation and discretisation of the continuity equation were discussed in the previous section. To validate the results from the continuity equation, we choose structures which can be solved for analytically. The analytical results are then compared to the simulations and the numerical error is plotted.

3.1.1 Linear resistor - Prism

A simple rectangular prism is considered to validate the continuity equation. The structure and its discretised form are shown in the figure below. The structure consists of two electrodes that completely cover the top and the bottom faces of the prism. This structure is chosen because a simple analytical expression can be used to relate the current in the device to the voltage, provided linear parameters for the material, such as the conductivity are known.

The current continuity equation reduces to a linear relationship between the potential applied to the electrodes and the current flowing through it as shown below. We

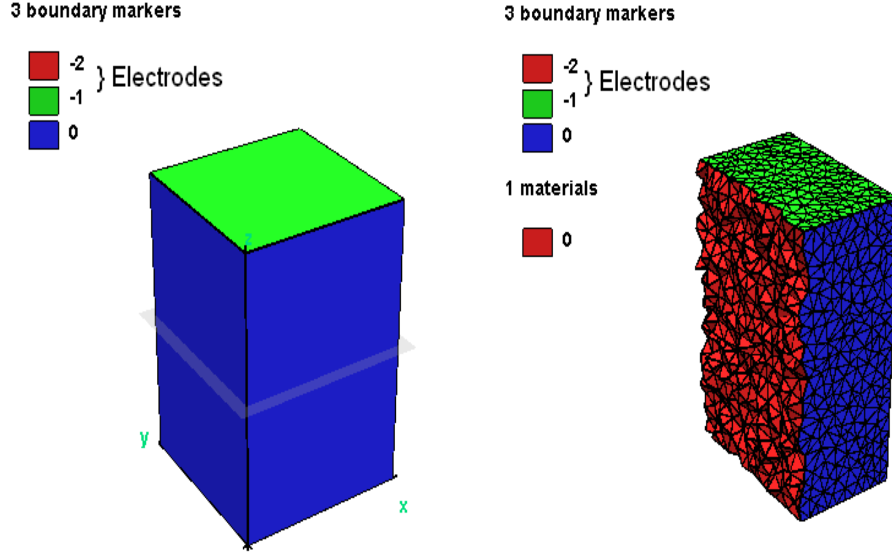

Figure 21: Rectangular prism with top and bottom electrodes

assume the conductivity σ to be homogenous and isotropic throughout the medium.

$$J = \sigma E$$
$$\frac{dI}{dA} = \sigma \frac{dV}{dz}$$

where the z direction is perpendicular to the plane of the electrodes and A is the area of the x-y plane. Since there is a constant potential drop and the current distribution is uniform along the x-y plane, we have

$$\frac{I}{A} = \sigma \frac{V}{L}$$
$$I = \frac{\sigma A V}{L}$$

For the above structure $A = 2.0 \times 10^{-6} \quad \times \quad 2.0 \times 10^{-6} = 4.0 \times 10^{-12} m^2$, $\sigma = 250\ \Omega^{-1} m^{-1}$ and $L = 3.0 \times 10^{-6} m$. The current is plotted below for various external voltages. The plot includes both the simulated current and the current calculated using the analytical expression.

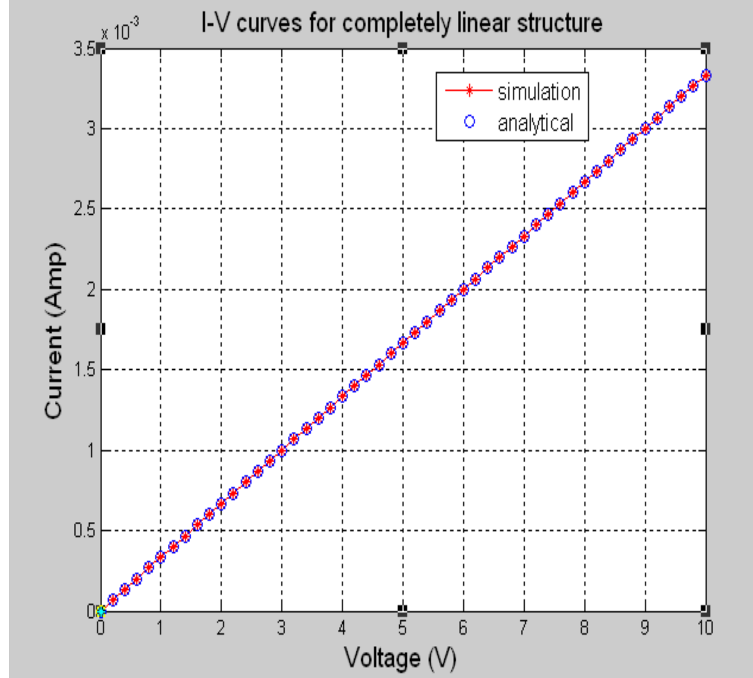

Figure 22: I-V curves for the linear device: Simulation and Analytical plots

The simulation values for the current are in close agreement with the analytically obtained results. A better comparison is made in Figure 23 which depicts the relative error between the two plots. The error is calculated as

$$\%error = \frac{|I_{simulation} - I_{analytical}|}{\frac{(I_{simulation}+I_{analytical})}{2}} \times 100 \tag{35}$$

As it can be seen from Figure 23, the relative error is on the order of $3 \times 10^{-11}\%$. The number of nodes used for the mesh was 4373. The potential distribution in the entire device is provided in Figure 24 for an external voltage of 5.0 Volts. Figure 25 shows the iso-surfaces in the potential distribution. Iso-surfaces help in validating the potential in the interior of the 3D device.

3.1.2 Linear resistor - Spherical quadrant

In the previous section, the symmetry and uniformity of the device in the x-y plane allows a 1-D simulation of the device without loss of accuracy. Here, we consider a

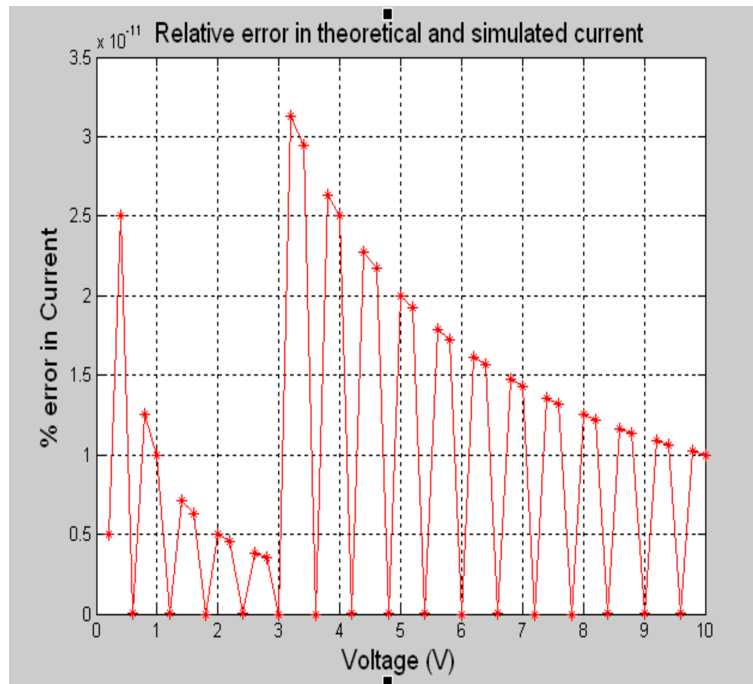

Figure 23: Relative error in current for the simulation of the linear device

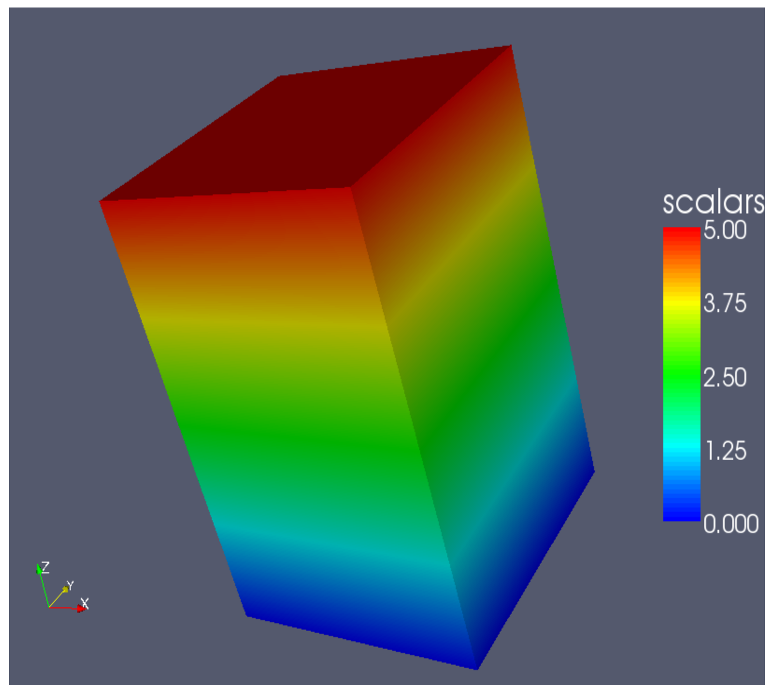

Figure 24: Potential distribution for a linear device

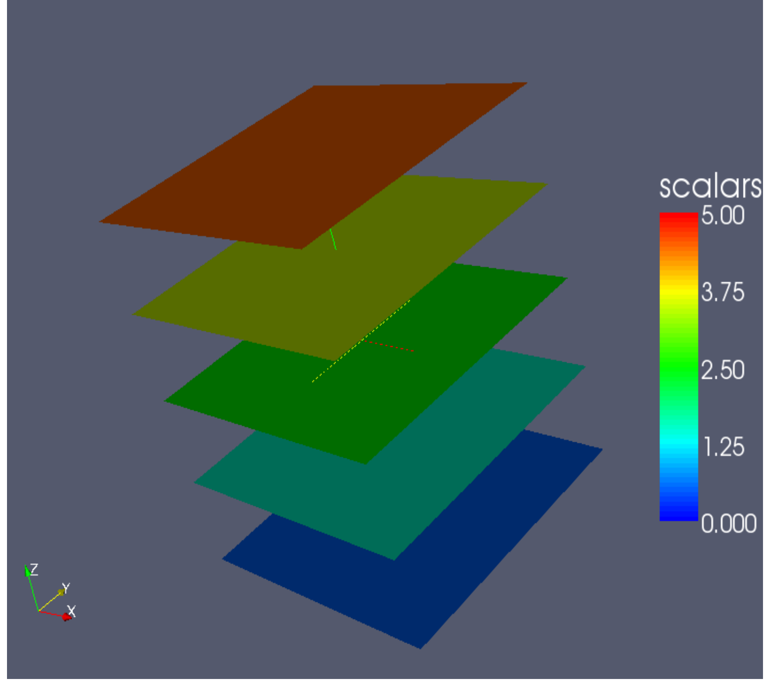

Figure 25: Iso surfaces for the potential at V = 0.5,1.5,2.5,3.5 and 4.5 Volts

device which can also be analytically solved, but requires a 3D simulation in Cartesian co-ordinates. Figure 26 shows a $1/8^{th}$ of a spherical shell with electrodes on the inner and outer surfaces. Due to the spherical symmetry of the device we can also obtain analytical results for the potential along the radial direction.

Parameter	Value
Inner radius(R1)	0.5 μm
Outer radius(R2)	1.0 μm
$Conductivity(\sigma)$	2.0 $\Omega^{-1}m^{-1}$
Potential difference(V)	1.0 V
Number of nodes	3044

Table 1: Dimensions for the spherical structure

The potential distribution for the spherical shell is given below. The external potential applied is 1.0 V. The potential distribution has a spherical symmetry that is apparent from the figure. The iso surfaces are shown in Figure 28

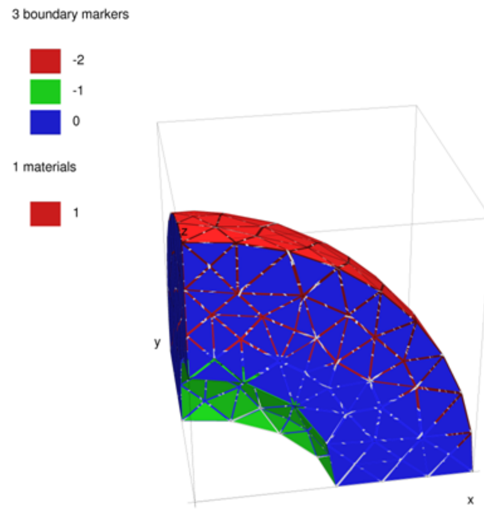

Figure 26: Discretised spherical structure. The red and green surfaces represent the electrodes.

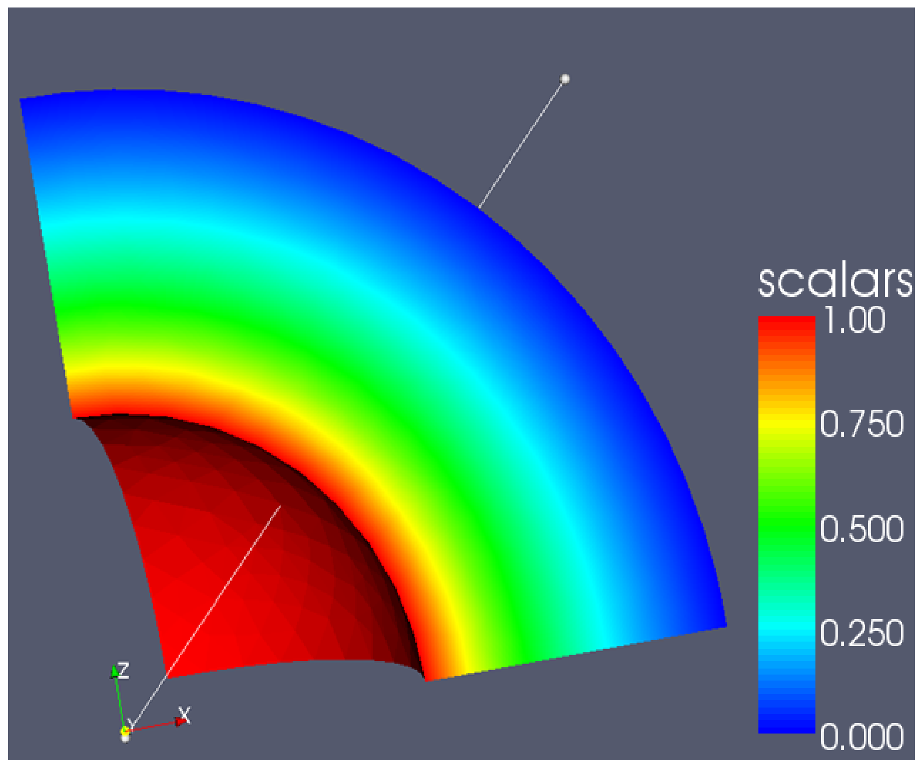

Figure 27: Potential distribution in the spherical structure

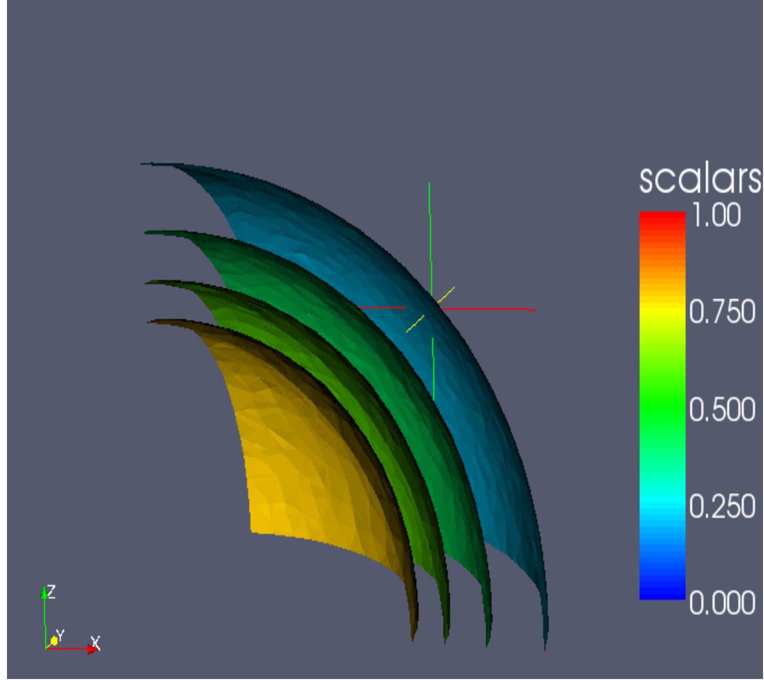

Figure 28: Iso surfaces in the spherical structure at V = 0.2,0.4,0.6 and 0.8 V

The analytical expression for the variation of the potential along the radial direction (the line shown in Figure 27) is given by

$$\phi(r) = \frac{A}{r} + B$$

where A and B are determined by the boundary conditions $\phi(0.5) = 1.0V$ and $\phi(1.0) = 0V$. Figure 29 below is a plot of the potential along the radial direction. The red markers denote the analytical result and the black line denotes the simulated result.

The simulated and the analytical results agree with each other. These tests validate the box integration method of solving the linear current continuity equation in the bulk region of the laser. Figure 30 depicts another structure where it would be difficult to perform simulations in 1D or 2D to obtain the potential distribution. Since the Photonic crystal VCSEL consists of defects and cavities of arbitrary geometries, the 3D simulation technique will help us analyze the structure.

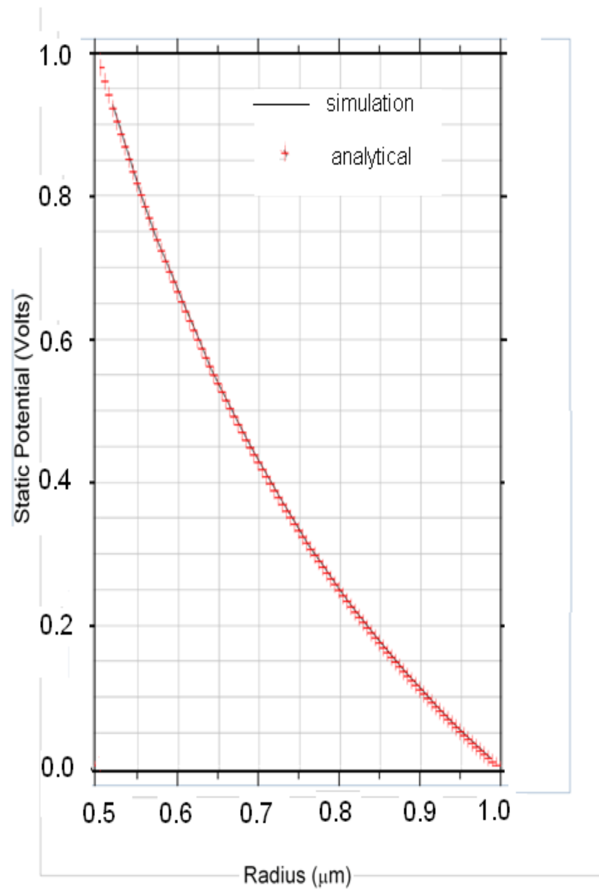

Figure 29: Potential distribution along the radial direction

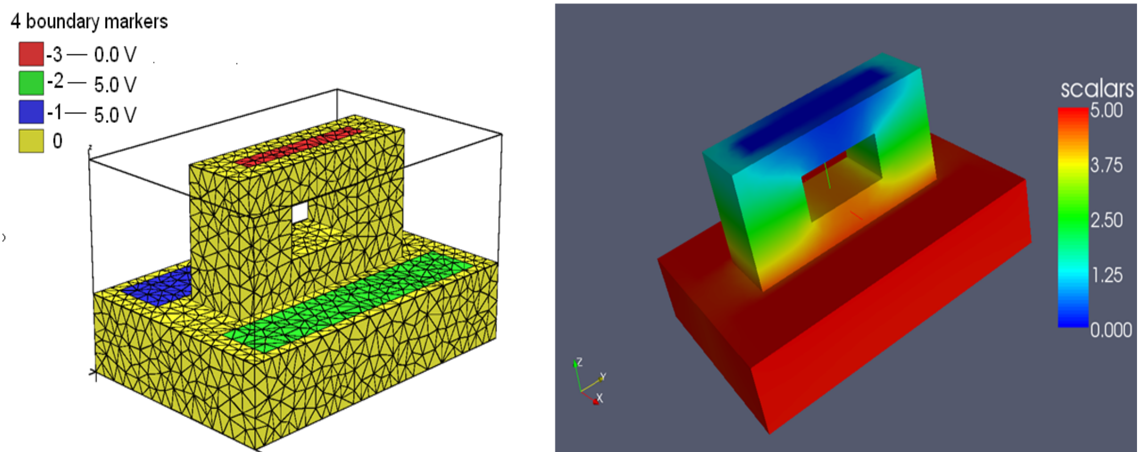

Figure 30: Discretised structure and its potential distribution

3.2 Validation of the active resistor model

The active resistor model is introduced to model the non linear layer in the device. The model is first validated for a case which can be solved for analytically.

3.2.1 Simple diode with large electrodes

This structure simulates a typical semiconductor diode with p and n regions and the active region in between. The top and bottom surfaces act as electrodes and this enables us to calculate the current through the device using analytical techniques. The effective resistor model is described in Section 2.1.2.1. The parameters used for this model are provided in Table 2.

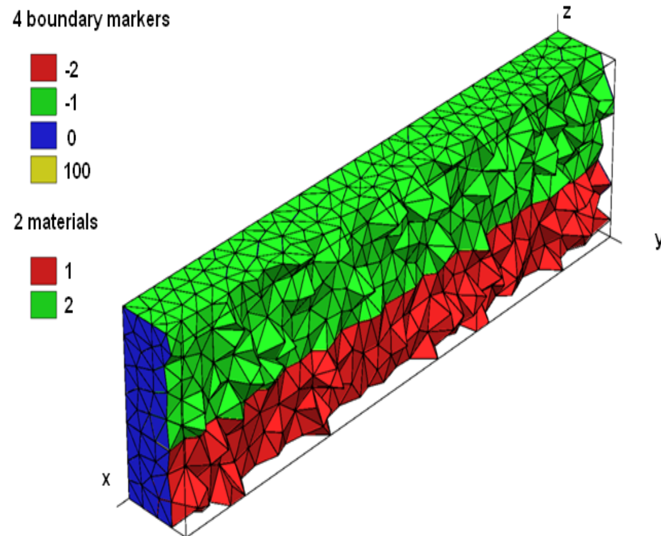

Figure 31: Structure used to for diode simulation. The plane between the two interfaces is used to simulate the active region.

Analytical calculations are performed using classical techniques, to obtain the current in the device. The current calculation can be done using either the Fermi-Dirac or the Maxwell-Boltzmann statistics for the carriers in the conduction and valence bands.Although the code normally uses the Fermi-Dirac statistics, it also has an option to use Maxwell Boltzmann statistics. The usage of Maxwell Boltzmann

Parameter	Value
L_x	20 μm
L_y	2.5 μm
L_{zt} (height of the top region)	3 μm
L_{zb} (height of the bottom region)	2 μm
Conductivity (σ) of top region	2.5 $\Omega^{-1}cm^{-1}$
Conductivity (σ) of bottom region	2.5 $\Omega^{-1}cm^{-1}$
Number of nodes	1619

Table 2: Dimensions for the diode structure

```
% parameters for the active resistor

Acoef = 0.0          1/sec
Bcoef = 1.4e-10     cm^3/sec
Ccoef = 0.0;        cm^6/sec
Dcoef = 2.5e-6;     cm^3/sec

Nc = 4.35e+17   1/cm^3
Nv = 8.31e+18   1/cm^3
Ntransp   = 1.0e18   1/cm^3

Egap = 1.25         eV
kT   = 0.026;       eV

width=0.14e-4;      cm

lin_res  = 0        0 for nonlinear, other for linear
J_over_U = 1e5     1/(Ohm cm^2)
```

Figure 32: Inputs for the effective resistor model. Provided in a file to the simulator

statistics allows us to arrive at a consistent formulation for the potential as a function of current. This is given by

$$V(I) = IR + E_g + kTlog(\frac{I}{AJ_0}) \tag{36}$$

where A is the area of the active resistor plane, $A = L_xL_y$, R is the linear resistance given by $R = \frac{L_{zt}+L_{zb}}{\sigma A}$ and $J_0 = q(width \times N_c \times N_v)$. The values for these parameters are listed in Table 2 and Figure 32. This analytical model assumes only the presence of spontaneous recombination and is valid only when the current densities are much larger than J_0. Nevertheless, the physical operating conditions of interest in a laser or LED lie in this range and hence we can use this model for comparison. The plots for current vs voltage are provided in the Figure 33. The simulation is performed for both the Maxwell-Boltzmann and Fermi-Dirac statistics. The analytical calculations are made using the Maxwell-Boltzmann statistics and plotted alongside.

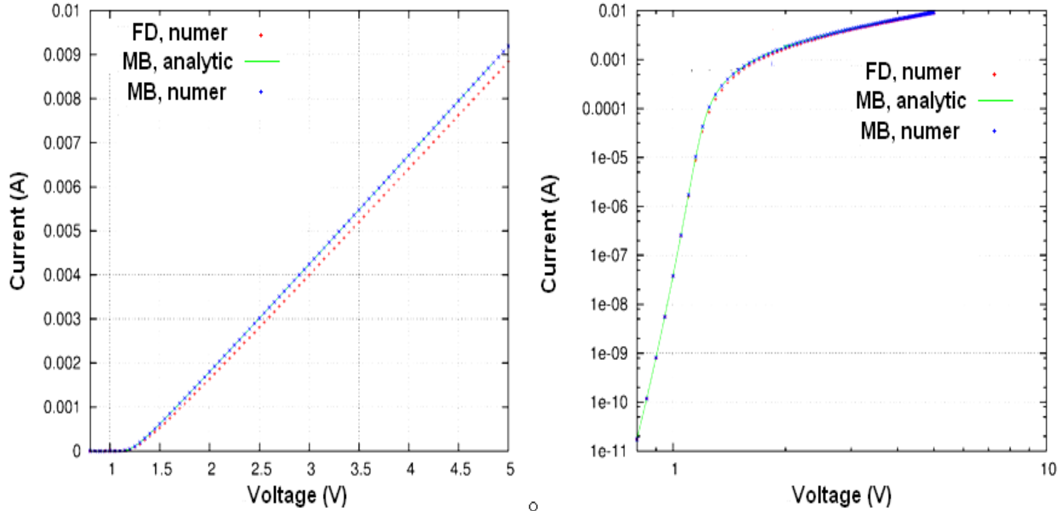

Figure 33: I-V curves for the diode. Linear and Logarithmic scales
FD - Fermi Dirac statistics. MB - Maxwell Botzmann statistics

Since at low biases, the carrier concentrations are also low, both the statistical distributions provide similar results and hence the current is also similar. As expected, the current differs at higher biases where the distributions provide different results.

3.2.2 Modeling Symmetrical structures

Although device structures may not have a uniform geometry along an entire axis, many structures possess symmetry around one of the axes (typically the growth axis). In this case it is advantageous to simulate only a part of the structure and extend the results to the symmetrical regions.As a quick and simple example the Figure 34 shows the laser diode on the left, and half of the discretised structure to the right.

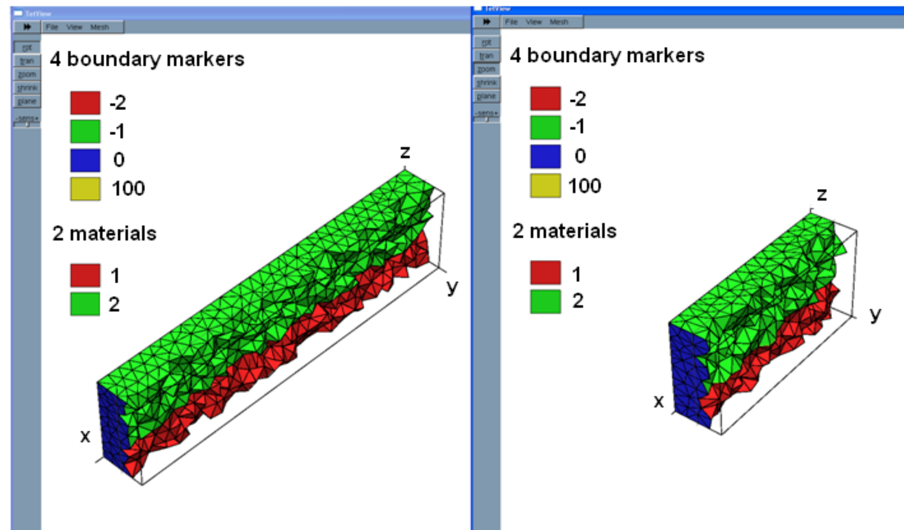

Figure 34: Laser diode, and half of the structure

As can be seen from Figure 35, it is sufficient to simulate the structure on the right. This allows better discretisation and more nodes can be used to discretise the same region.

3.3 VCSEL modeling

The VCSEL structure can now be analysed using the models and techniques described in previous sections. A simple VCSEL structure is as shown in Figure 36

The Distributed Bragg Reflectors, which are alternating layers of the semiconductor material are modelled as a lumped material. Since the conductivity is the only material parameter used for the bulk region, and since this is linear, we can assign

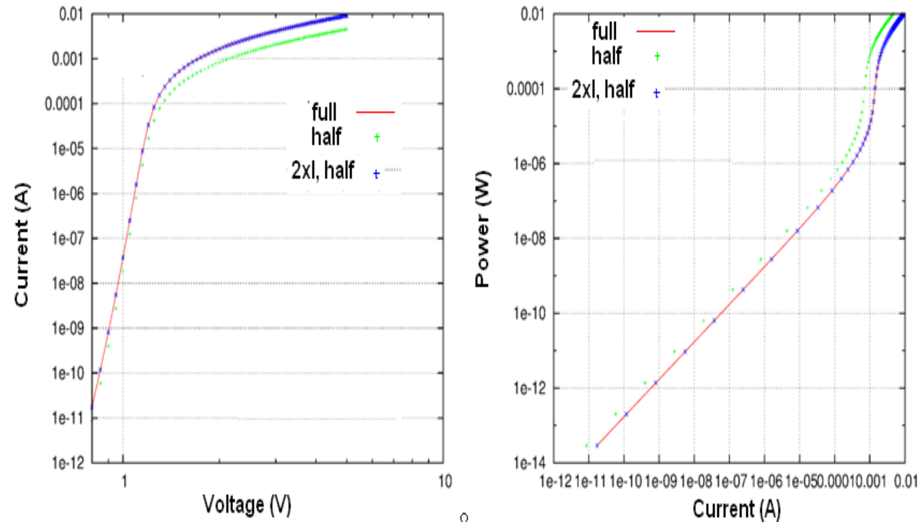

Figure 35: Comparison of I-V and L-I curves for full and half diodes on the logarithmic scale. The 2 × I implies that the current in the half diode was doubled.

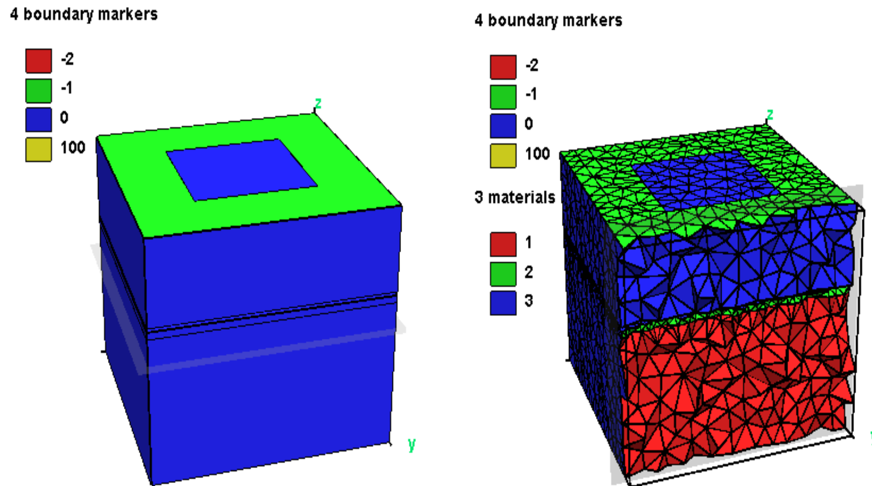

Figure 36: Simple VCSEL structure. The green portion at top represents the electrode.

average properties of the alternating layers to the lumped material. One can also model the heterojunctions between the semiconductor layers using non linear functions similar to the active layer modeling. It can be noticed that the structure in Figure 36 is symmetric about the z axis. It is sufficient to model only $1/4^{th}$ of the above structure to study the VCSEL. This is depicted in Figure 37

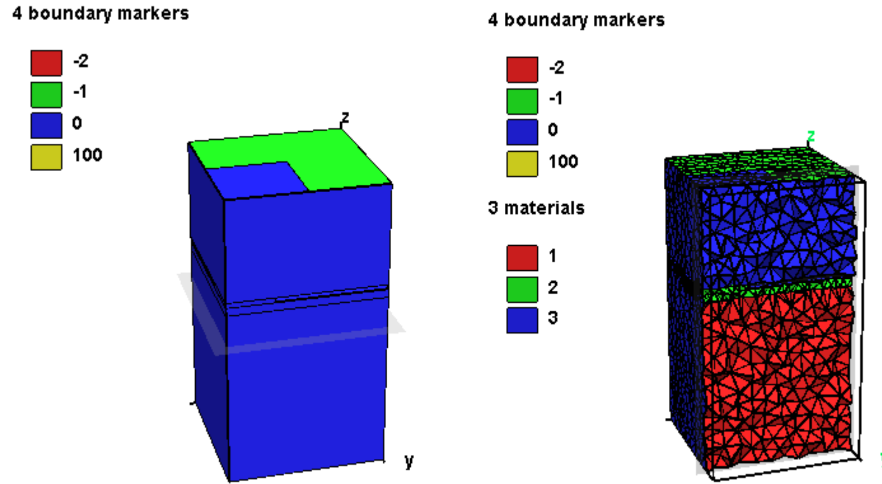

Figure 37: $1/4^{th}$ of the VCSEL structure

The $1/4^{th}$ VCSEL structure is elaborately described in Figure 37, which shows each part of the structure. The oxide region of the VCSEL helps in directing the current through active layer in the lateral direction. This region is modelled as a perfect insulator by removing the region from the meshed structure. Hence the region around the optical aperture is excluded from the device geometry. The active layer is present (modelled as a plane) just below the oxide region.

The mesh near the active region has higher refinement compared to the other regions. This is because there can be a high spread in the current density in the active region needs to be calculated accurately. The bottom face of the device is entirely covered with the second electrode. The dimensions and properties of the device are listed in Table 3

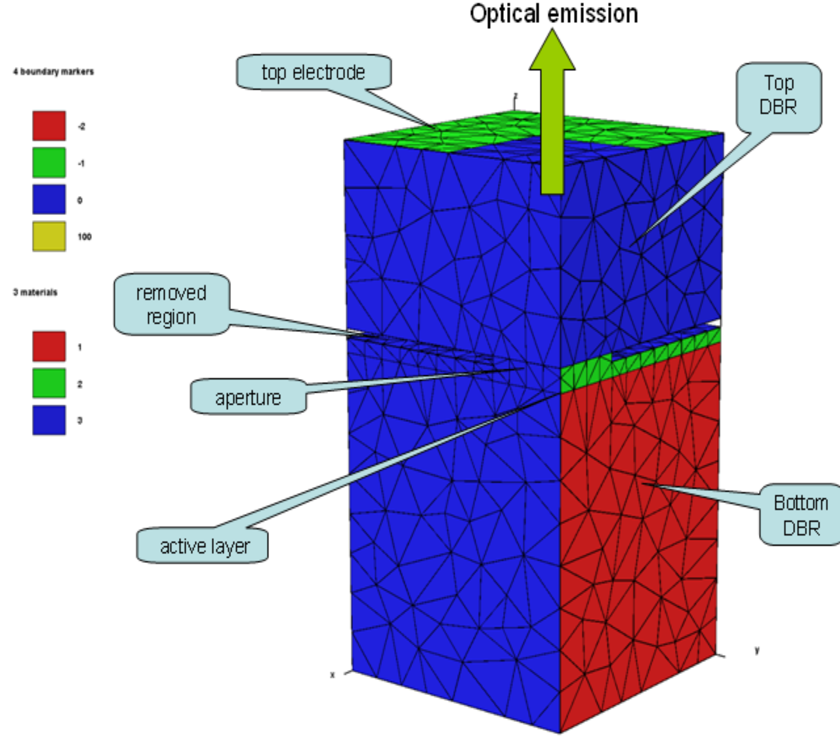

Figure 38: Description of the $1/4^{th}$ of the VCSEL structure

Parameter	Significance	Value
L_x	Length in x direction for $1/4^{th}$ VCSEL	5 μm
L_y	Length in y direction for $1/4^{th}$ VCSEL	5 μm
L_z	Height of the VCSEL	8.9310866 μm
Z_a	z co-ordinate of the active region	5.4517959 μm
Z_{ab}	z co-ordinate for the bottom of the aperture	5.7 μm
W_{ax}, W_{ay}	Width of aperture in x and y direction for $1/4^{th} VCSEL$	1.5 μm
W_{ex}, W_{ey}	Width of top electrode in x and y direction	2.5 μm
σ_{top}	Conductivity of regions 2 and 3	850 $\Omega^{-1}m^{-1}$
σ_{bottom}	Conductivity of region 1	12750 $\Omega^{-1}m^{-1}$
N_{nodes}	Number of nodes	1338

Table 3: Dimensions for the VCSEL structure

The conductivity of the DBR mirrors is selected to be within the range which is measured experimentally. The conductivity of the n-doped DBR is assumed to be 15 times larger than for the p-doped DBR.

We consider the simulation of the case where the active region is represented by the non linear active resistor model. This is coupled to the optical cavity where the dynamics is modelled using the photon rate equation.The confinement factors for the device are provided as an input to the simulator. The confinement factor distribution for the above geometry is shown in Figure 39. These factors are for the lowest order optical mode in the structure. These were calculated using an external optical solver based on the Transfer Matrix Method. The solver also calculates the cavity lifetime and the cavity resonance. For the above structure, these are 3.13 ps and 1.27 eV respectively.

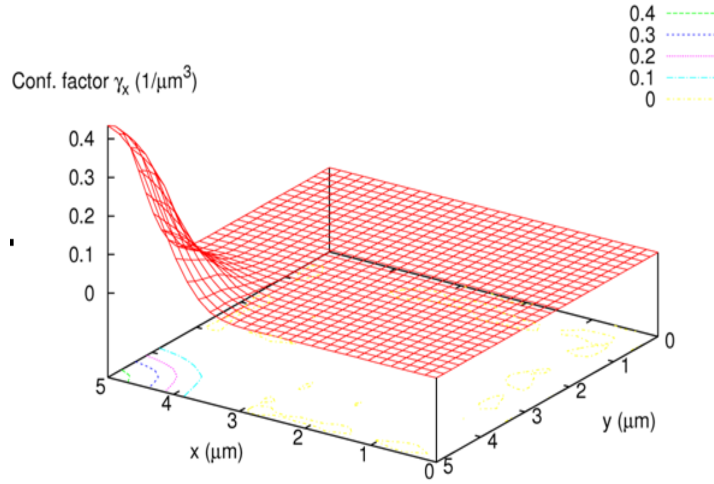

Figure 39: x-component of the confinement factors for the $1/4^{th}$ VCSEL structure

The injected currents and optical power for different potentials are plotted below. It should be noted that currently the active region is modeled as a double heterostructure. A more accurate modelling would be to use the quantum well approach and

the 2D density of states. However, as can be seen from the results, the currents and optical power lie in an acceptable range of accuracy.

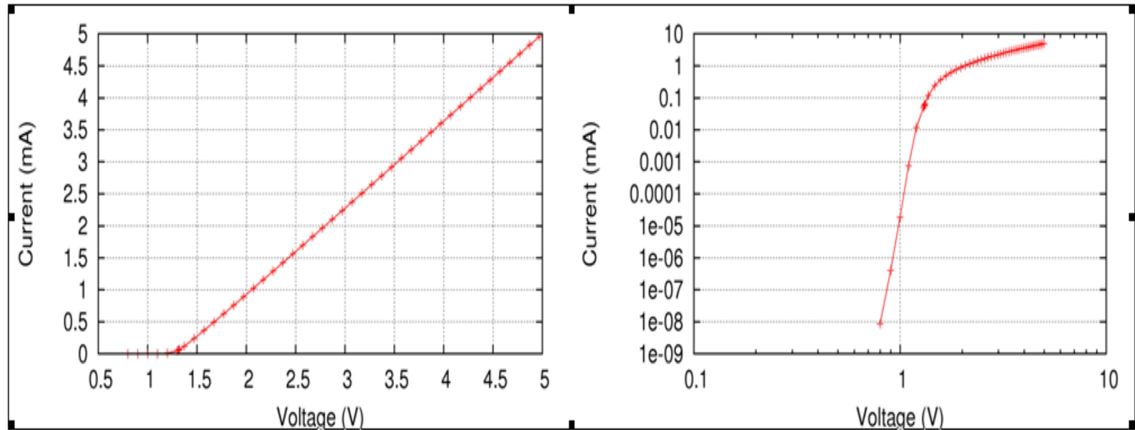

Figure 40: I-V plots for the $1/4^{th}$ VCSEL structure:linear and logarithmic scale

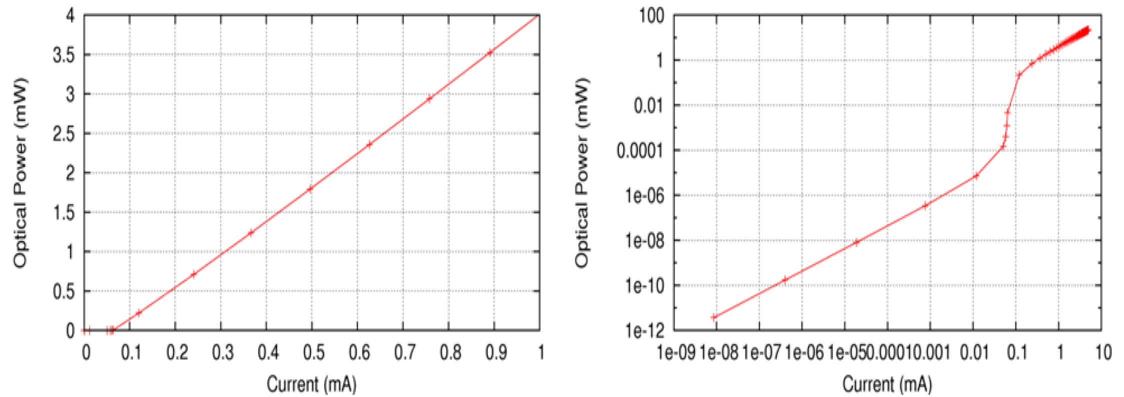

Figure 41: Plots of optical power for the VCSEL structure:linear and logarithmic scale. The optical power is for the entire VCSEL structure unlike the current.

The resistance of the linear part of the device can be calculated by taking the numerical derivative. This is 732.6 Ω. This resistance can be compared to the resistance obtained from experimental results. We consider an experiment performed on a very similar VCSEL where the I-V characteristics are obtained [40]. The aperture radius in the experiment was 1.7 μm. The current voltage characteristics are as shown in

Figure 42.

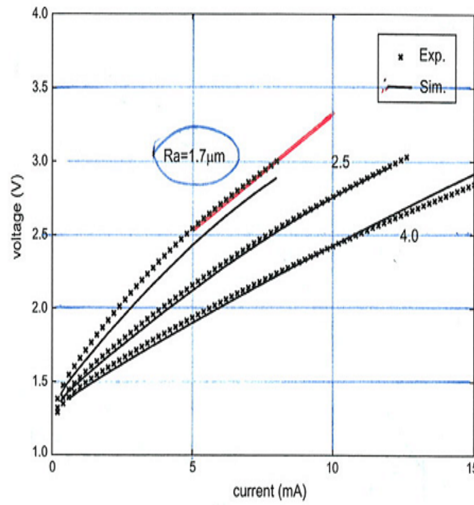

Fig. 8. Simulated and measured current-voltage characteristics for devices with aperture radii of 1.7, 2.5, and 4.0 μm.

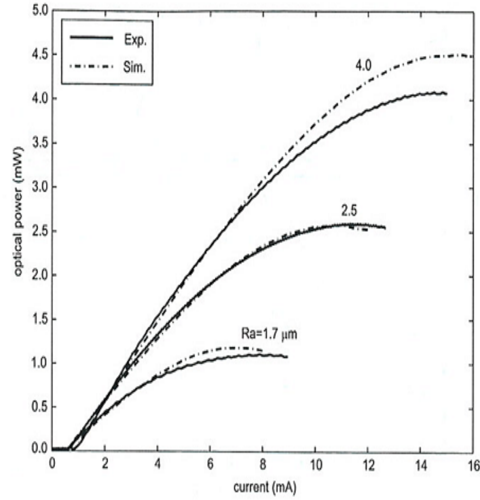

Fig. 9. Simulated and measure light-current characteristics for the same devices as in Fig. 8.

Figure 42: Experimental I-V and L-I curves for a similar VCSEL. From Liu et al [40]

The experimental results show a differential resistance of around 160 Ω in the linear region. In our simulations we obtained the resistance to be 732.6 Ω for the quarter structure or 183.16 Ω for the full structure. There is a discrepancy in the threshold current (0.6-0.8 mA in the experimental case as compared to 0.262 mA for the simulated case). In this simulation, Auger recombination and the linear recombination terms were not included. The threshold current increases on the inclusion of these terms.In addition to these, optical absorption, which is not modelled currently, is also responsible for increasing the threshold current. Optical absorption may also be responsible for the discrepancy in the optical output power. This is approximately 0.5 mW in the in the experiments, but as high as 1.8 mW in the simulation. Also, the optical power in the simulation is calculated for the entire device. In case of the experiments, it is calculated only at the top of the optical aperture i.e the optical

power obtained through the top mirror.

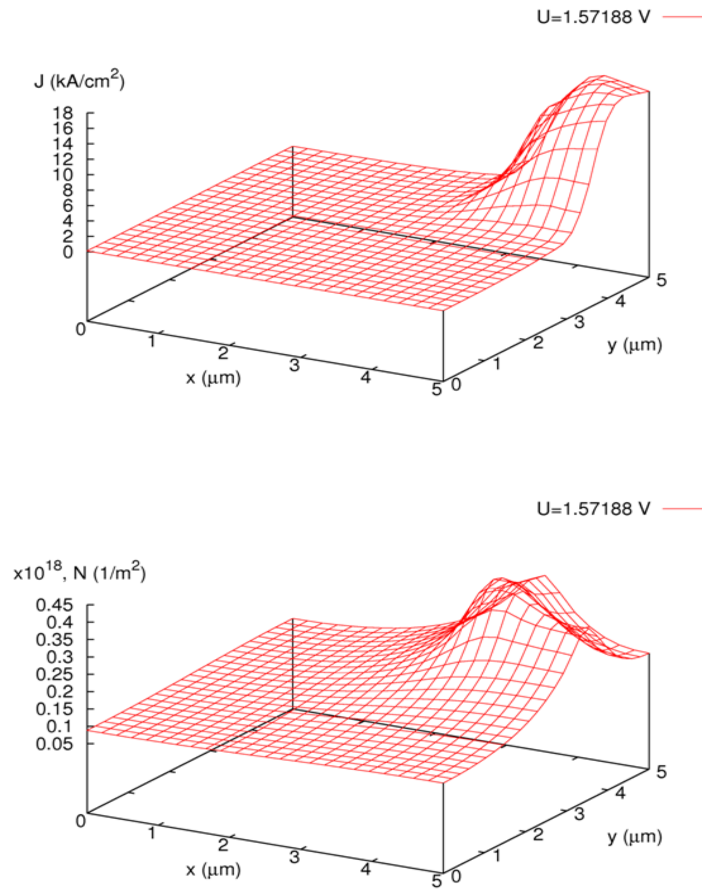

Figure 43: Simulation results : Distribution of current density and carrier density on active layer

Figure 43 shows the plots of current and carrier density on the active region. Both parameters represent 2D densities as the active region is approximated as a plane. The current density is typically concentrated near the aperture, due to current crowding effects. Above the laser threshold, the carrier density distribution is clamped at the center of the aperture. This is because the optical mode rapidly decreases away from the centre, hence allowing a higher carrier density at the edge of the aperture. Figure 44 compares the current density above and below laser threshold.

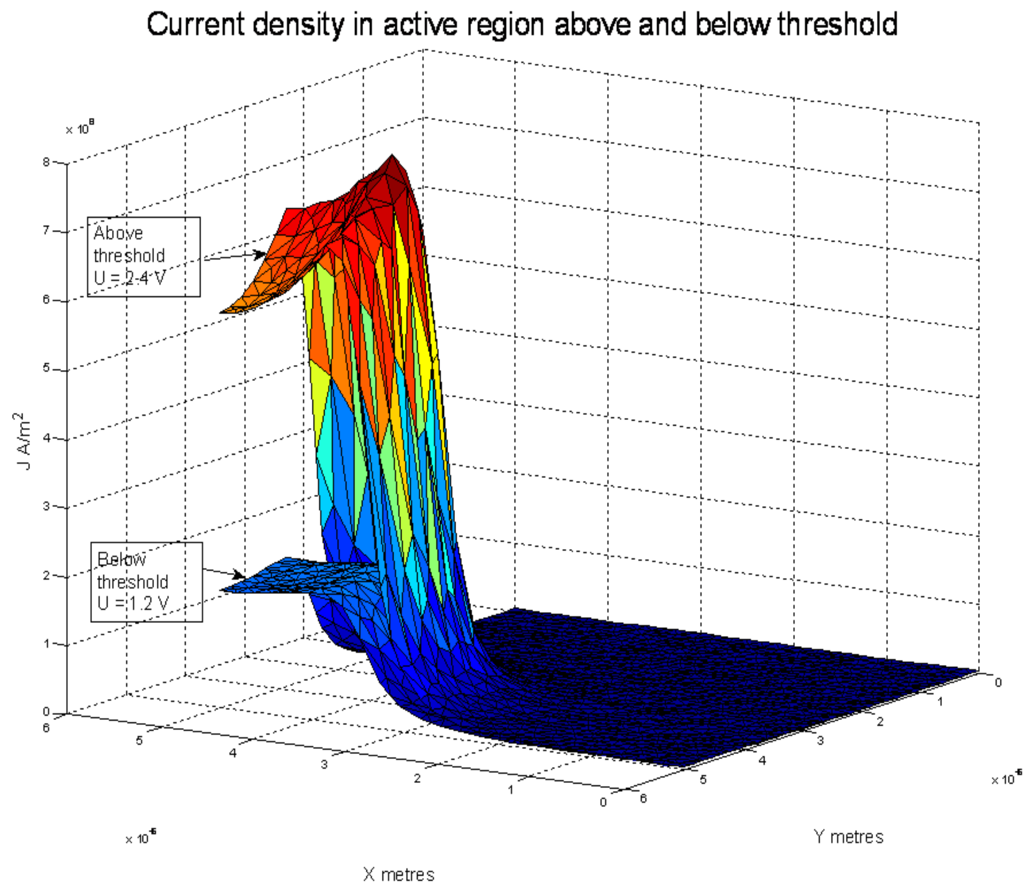

Figure 44: Comparison of current density in VCSEL above and below threshold

3.4 Photonic crystal VCSEL structures with defects

The advantages of such structures were discussed in Chapter 1. An analysis of such structures requires a 3D simulation. It is often advantageous to have a fast simulation technique to analyse the characteristics of the structure for varying dimensions. This aids the experimental process significantly, as exploring the design space via growth and characterisation for varying dimensions of the structure and defects is not practical.

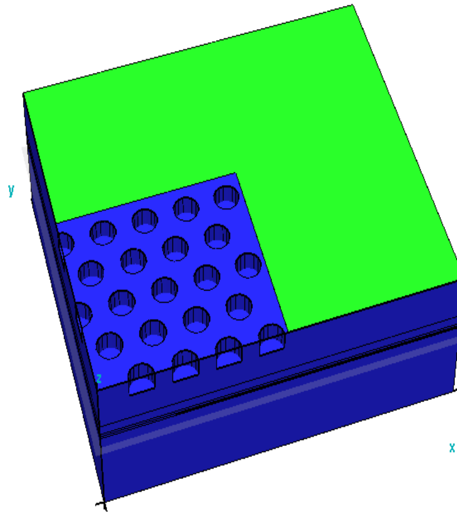

Figure 45: Photonic crystal VCSEL structure with defects

The characteristic resistance of this structure is important because the holes cause an increase in the resistance of the device, although they are advantageous to achieve single mode operation. A fast analysis of the impact of the diameter and depth of the holes on the resistance of the device was performed using our 3D simulator. The I-V charecteristic plots for varying hole sizes are shown in Figure 46.

3.5 Analysis of band to bound recombination model

The simulator can also be used to analyse the different models used in the active layer and to create fitting parameters from experiments for a particular model used. One

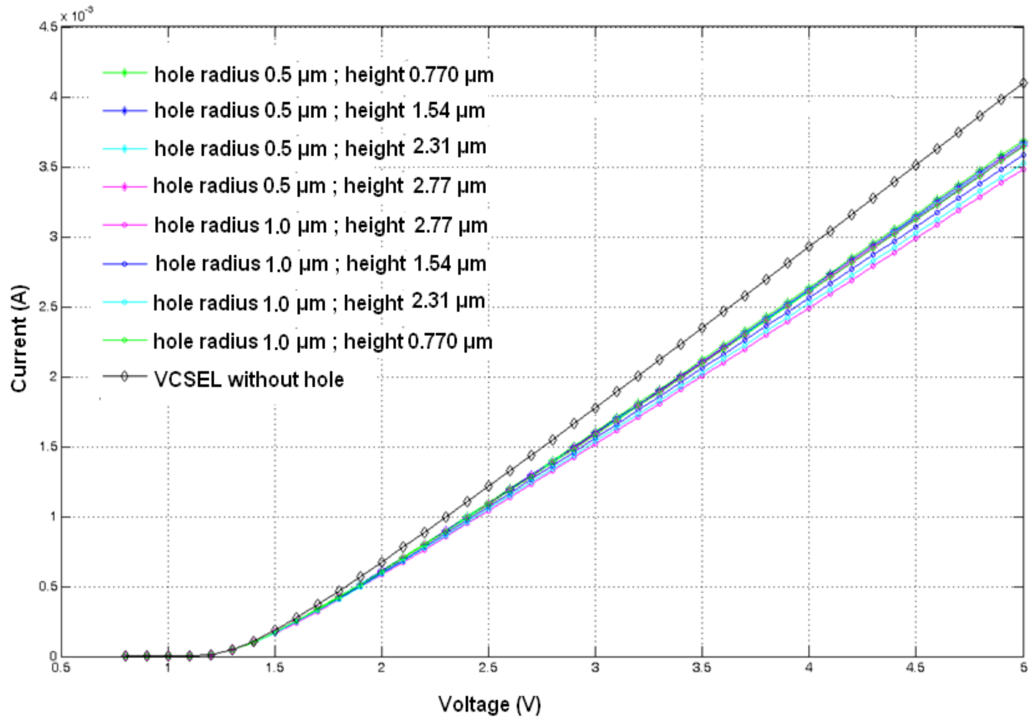

Figure 46: I-V plots for different defect dimensions

such analysis is described here. One of the non-radiative recombination processes, the band to bound recombination models the recombination due to carriers that fall into impurity states in the band gap. This type of recombination is proportional to the carrier density. This can be expressed as

$$R_{nr} = dAN \tag{37}$$

where d is the width of the active region,A is proportionality constant or the defect state recombination coefficient and N is the carrier concentration in the active region. The simulation results can be used calculate A as a fitting parameter from experiment. The plots of the cavity photon number for various A coefficients are provided here for the $1/4^{th}$ VCSEL structure.

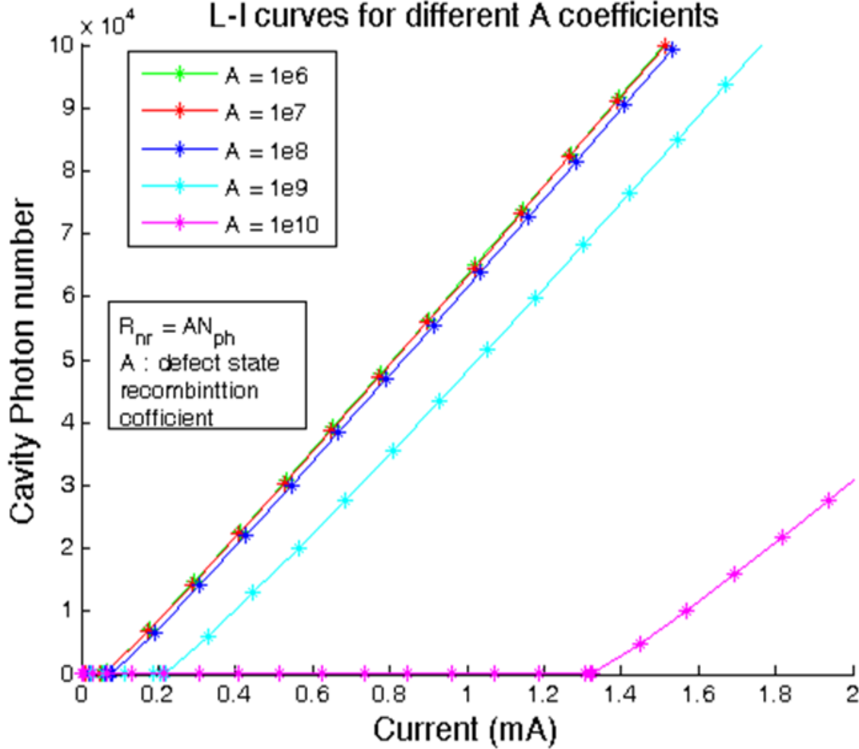

3.6 Performance analysis of the simulator

The advantage of having a low cost modular simulator is the low time and processing resource requirement in running simulations. The Newton iterations involve a linear step wherein the error is estimated by computing the inverse of the Jacobian of the system. This matrix operation involves 2D arrays for the number of nodes and the number of double points on the interface. This is quite a burden on the memory and time requirements if a regular matrix solver is used. Fortunately, since the mesh structure involves coupling only between the neighbouring nodes, the matrix is sparse. Sparse matrix solvers reduce the memory and time requirements by a considerable amount. The sparse matrix solver used in the implementation of the simulator is the PARDISO solver [4] which is also a part of Intel's MKL library. The solver uses a sparse format as described in the manual[3]. Using this format, we only need to store the non zero elements of the matrix and the a couple of other matrix of order N_{nodes}.

This is a significant improvement over the full storage of the matrix which is of the order of N^2_{nodes}. Table 4 demonstrates the advantage of the sparse matrix solver over the regular dgesv matrix solver.

Number of nodes	Number of points on active layer	Matrix size Dgesv solver	Matrix size Pardiso	Time Dgesv solver	Time (Pardiso)
1180	237	2007889	18883	488.73 seconds	13.6 seconds
1778	271	4198401	26225	1175.52 seconds	18.62 seconds
2456	338	7806436	37845	2707.61 seconds	29.07 seconds
3029	408	11812969	49564	5351 seconds	41.23 seconds

Table 4: Comparison of CPU times for different solves

These results were obtained for the $1/4^{th}$ VCSEL structure on a 3.00 GHz Intel Xeon processor with 1GB RAM.

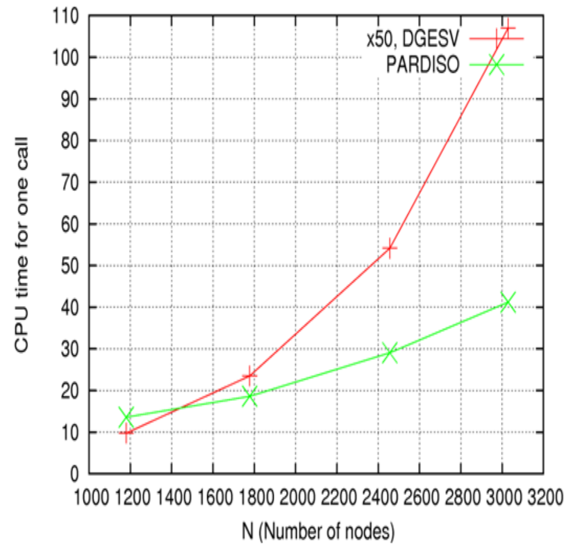

Figure 48: Comparison of CPU time for DGESV and PARDISO solvers

The usage of the sparse matrix solvers allows a reasonable simulation time and memory even for very large mesh sizes. The simulation times for $1/4^{th}$ VCSEL structure for mesh sizes up to 80,000 nodes are provided in Table 5.

Num nodes	Num active layer points	One call of solver	Full simulation
1180	237	0.03 seconds	13.6 seconds
1778	271	0.05 seconds	18.62 seconds
2456	338	0.08 seconds	29.07 seconds
3029	408	0.115 seconds	41.23 seconds
3784	498	0.15 seconds	59.08 seconds
4565	619	0.19 seconds	124.2 seconds
7149	903	0.37 seconds	156.96 seconds
13713	1297	1.09 seconds	456.48 seconds
25228	1596	2.94 seconds	1257.91 seconds
42811	3691	6.01 seconds	2632.45 seconds
75450	5968	15.84 seconds	6922.64 seconds

Table 5: CPU times for different number of nodes in the CPU solver

CHAPTER IV

CONCLUSION

Photonic crystal LED and VCSEL simulation requires a 3D simulation to model the essential features of the problem. A full fledged semiconductor modelling of the entire device is computationally intensive and slow, and a simpler approach is desired. In this paper, we present such a model. The device is separated into bulk and active regions, and simplified models appropriate for each region are applied. Three dimensional models can be used to model the bulk regions of the device using bulk parameters such as conductivity. Since current flow is mainly in the vertical direction in the active region of the device, the active region can be modelled by resistors which carry current in the vertical directions and whose resistance is related to the potential drop using a non linear functional depending on the electrochemical potentials in the heterostructure region. As shown in the results, such a model provides a reasonable comparison with experimental data even in its primitive form. The model can be further improved by simulating the active region more accurately (perhaps by performing a drift diffusion simulation in the active region). The existing simulator has low computation complexity with simulation times ranging from 124 seconds for a 4500 node problem to 1200 seconds for a 25000 node problem on a 3. 00GHz, 1GB sequential Linux machine.

4.1 Future Work

Although the framework of the simulator has been satisfactorily developed, modularity of varying complexity needs to be achieved by the use of different models, particularly for the active region. The investigation of current spread in Nitride LEDs and lasers requires the modeling of prominent physical effects such as strain

and polarization. Some of the alternate models for the active region that are in the development stage are mentioned here.

4.1.1 k.p.model

The electronic bound states within the quantum well are required to obtain an accurate expression for the carrier density dependent optical gain G and spontaneous emission coefficient A. To obtain these states, a finite-difference 8 band quantum well k. p solver including strain and polarization fields (in nitride devices) has been developed and implemented by Venkatachalam et.al[60]. Coding to include the carrier-density-dependent screening (Hartree term) in the Hamiltonian is ongoing, in order to more accurately calculate the optical gain.

4.1.2 Drift-Diffusion model

The drift diffusion model provides a more rigorous approach to obtaining the current density in the active region. This model itself can have varying levels of approximation with a 1D, 2D or full fledged 3D approach to the device. In the 1D case, an approach similar to the active resistor model is used, but discretisation is performed in the vertical direction in the active layer, and the drift - diffusion equations are solved for each section (modeled as a 1D region) in the active layer. This code is currently under development. Existing commercial and academic drift diffusion models in 1D regions include SimWindows [7] and Silense[6] (for nitrides). Further a quasi 3D approach involving multiple 2D layers or a full fledged 3D model may be used to achieve higher accuracy. However, this would require significant increase in computational resources and time, compromising the desired efficiency of the simulation.

4.1.3 Efficient optical solver

In this work, a planewave expansion based modal method developed by Krishnamurthy et.al[35, 36] is used to solve Maxwells equations for the optical modes throughout the structure. In this method, the 3D structure is first split into various 2D slices which are uniform along the out-of-plane direction. Modes are calculated in each 2D slice and are propagated along outof-plane direction through the use of scattering matrices [37, 14]. The usage of planewaves for expansion of modes enable us to embed Fourier operator directly into Maxwells equations solver rendering the solver matrix-free. So computationally O(Nlog(N)) operations are performed and O(2N) storage space is needed if N is the number of grids. The solver has been tested for various structures.Presently the solver is being integrated for photonic crystal defect based VCSELs and LEDs.

The various models need to couple with each other to provide self consistent solutions. In case the modules work independently on inputs from other modules in an iterative manner, the equations would be solved in a decoupled manner. In such a case, the Gummel iteration scheme [52] can be used as an the iterative technique in solving the decoupled system.

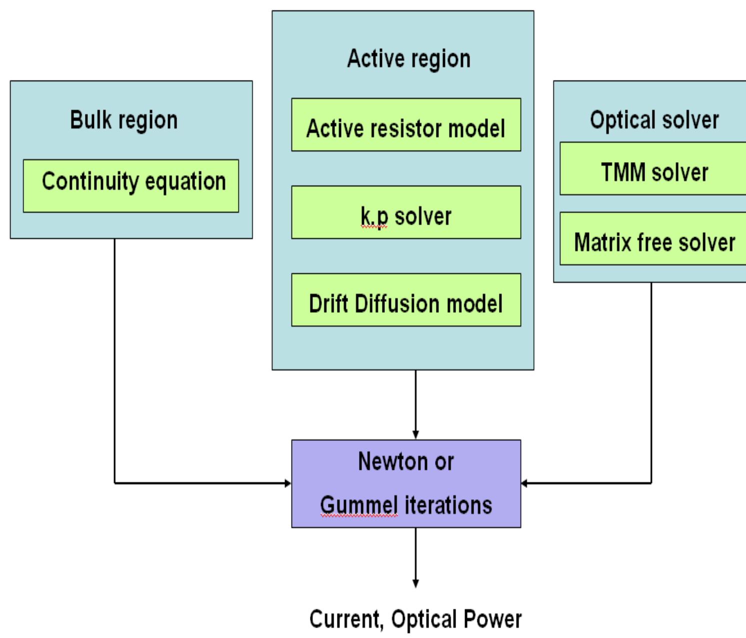

Figure 49: Modular depiction of the 3D simulator

REFERENCES

[1] "Crosslight Software Product Overview." "http://www.crosslight.com/Product_Overview/prod_overv.html".

[2] "Demands for the Box Integration Method." " http://www.iue.tuwien.ac.at/phd/cervenka/node12.html".

[3] "PARADISO Solver Manual." "http://www.pardiso-project.org/manual/manual.pdf'.

[4] "PARADISO Solver Project." "http://www.pardiso-project.org/".

[5] "The Poisson Equation." " http://www.iue.tuwien.ac.at/phd/cervenka/node16.html".

[6] "Simulator for Light Emitters based on Nitride Semiconductors." "http://www.semitech.us/products/SiLENSe/".

[7] "SimWindows Semiconductor Device Simulator." "http://www.simwindows.com/".

[8] "Tcad Sentaurs Device Optoelectronics." " http://www.synopsys.com/products/tcad/sentaurus_devopto_ds.html".

[9] "Tetgen, A Quality Tetrahedral Mesh Generator and Three-Dimensional Delaunay Triangulator." "http://tetgen.berlios.de/".

[10] "Tibercad multiscale device simulator." " http://www.tibercad.org/".

[11] Auf der Maur, M., Povolotskyi, M., Sacconi, F., and Di Carlo, A., "Tibercad: A new multiscale simulator for electronic and optoelectronic devices," *Superlattices and Microstructures*, vol. 41, no. 5-6, pp. 381 – 385, 2007.

[12] Bank, R. E. W., Coughran Jr, M., Driscoll, M. A., Smith, R. K., and Fichtner, W., "Iterative methods for semiconductor device simulation," *Computer Physics Communications*, vol. 53, pp. 201–212, May 1989.

[13] Bank, R., Rose, D., and Fichtner, W., "Numerical methods for semiconductor device simulation," *Electron Devices, IEEE Transactions on*, vol. 30, pp. 1031–1041, Sep 1983.

[14] Bienstman, P. and Baets, R., "Rigorous and Efficient Optical VCSEL Model based on Vectorial Eigenmode Expansion Perfectly Matched Layers," *Optoelectronics, IEE Proceedings*, vol. 149, no. 4, pp. 161–165, 2002.

[15] Bissessur, H., Koyama, F., and Iga, K., "Modeling of oxide-confined vertical-cavity surface-emitting lasers," vol. 3, (Haifa, Israel), pp. 344 – 52, 1997/04/.

[16] Chew, L., "Constrained delaunay triangulations," *Algorithmica*, vol. 4, no. 1, pp. 97 – 108, 1989//.

[17] Choquette, K., "Vertical-cavity surface-emitting lasers: light for the information age," *MRS Bull. (USA)*, vol. 27, no. 7, pp. 507 – 11, 2002/07/.

[18] Choquette, K. and Hou, H., "Vertical-cavity surface emitting lasers: moving from research to manufacturing," *Proceedings of the IEEE*, vol. 85, no. 11, pp. 1730 – 9, 1997/11/.

[19] Danner, A., Raftery, J.J., J., Leisher, P., and Choquette, K., "Single mode photonic crystal vertical cavity lasers," *Applied Physics Letters*, vol. 88, no. 9, pp. 91114 – 1, 2006/02/27.

[20] Evstratov, I., Mymrin, V., Karpov, S., and Makarov, Y., "Current crowding effects on blue led operation," *Physica Status Solidi C*, no. 6, pp. 1645 – 8, 2006//.

[21] Frederick, C., Wong, Y., and Edge, F., "Two-dimensional automatic mesh generation for structural analysis," vol. 2, no. 1, pp. 133 – 44, 1970.

[22] Grupen, M., "Simulating carrier dynamics in quantum well lasers," vol. 2693, (San Jose, CA, USA), pp. 374 – 85, 1996//.

[23] Grupen, M. and Hess, K., "Simulating the modulation response of quantum well laser diodes," (St. Petersburg, Russia), pp. 641 – 6, 1997//.

[24] Grupen, M. and Hess, K., "The coupled optoelectronic problems of quantum well laser operation," vol. 6, (Tempe, AZ, USA), pp. 355 – 62, 1998//.

[25] Grupen, M. and Hess, K., "Simulation of carrier transport and nonlinearities in quantum-well laser diodes," *IEEE Journal of Quantum Electronics*, vol. 34, no. 1, pp. 120 – 140, 1998. Carrier capture;Spectral hole burning;Helmholtz equation;Bethe thermionic emission theory;.

[26] Hess, K., "Simulation of carrier transport and hot phonon effects in quantum well laser diodes," (Leuven, Belgium), pp. 275 –, 1998//.

[27] H.Haug and S.W.Koch, *Quantum Theory of Optical and Electrical Properties of Semiconductors*. World Scientific, 1994 (Third edition).

[28] Holonyak, N., J., "The semiconductor laser: a thirty-five-year perspective," *Proceedings of the IEEE*, vol. 85, no. 11, pp. 1678 – 93, 1997/11/.

[29] Iga, K., "Vertical-cavity surface-emitting laser: Its conception and evolution," *Japanese Journal of Applied Physics, Part 1: Regular Papers and Short Notes and Review Papers*, vol. 47, no. 1, pp. 1 – 10, 2008.

[30] Joe, B., "Construction of three-dimensional delaunay triangulations using local transformations," *Computer-Aided Geometric Design*, vol. 8, no. 2, pp. 123 – 42, 1991/05/.

[31] Karpov, S., Bulashevich, K., Mymrin, V., Zhmakin, I., and Zhmakin, A., "Simulation of visible and ultra-violet group-iii nitride light emitting diodes," *Journal of Computational Physics*, vol. 213, no. 1, pp. 214 – 38, 2006/03/20.

[32] Klein, B., Register, L. F., Grupen, M., and Hess, K., "Numerical simulation of vertical cavity surface emitting lasers," *Optics Express*, vol. 2, no. 4, pp. 163 – 168, 1998.

[33] Klein, B., Register, L. F., Hess, K., Deppe, D. G., and Deng, Q., "Active cavity modes for vcsel simulation," *Proceedings of SPIE - The International Society for Optical Engineering*, vol. 3627, pp. 78 – 86, 1999.

[34] Kosinovsky, G., Grupen, M., and Hess, K., "Effect of carrier charge imbalance on the threshold current in diode lasers with thin intrinsic quantum wells," *Applied Physics Letters*, vol. 65, no. 25, pp. 3218 – 20, 1994/12/19.

[35] Krishnamurthy, V., Messer, M., Allen, J. K., and Klein, B., "Matrix-Free Plane Wave based Modal Approach for Robust Design of Photonic Structures," *CLEO/QELS 2008 Poster no. JThA95*, May, 2008.

[36] Krishnamurthy, V. and Klein, B., "Planewave Expansion based Eigenmode Method for Scattering Matrix Analysis of Photonic Structures," *Journal of Optical Society of America(To be submitted)*.

[37] Lalanne, P. and Silberstein, E., "Fourier-modal Methods Applied to Waveguide Computational Problems," *Opt. Lett.*, vol. 25, no. 15, pp. 1092–1094, 2000.

[38] Lawson, C. L., "Properties of n-dimensional triangulations," *Comput. Aided Geom. Des.*, vol. 3, no. 4, pp. 231–246, 1987.

[39] Liu, Y., Ng, W.-C., Oyafuso, F., Klein, B., and Hess, K., "Simulating the modulation response of vcsels: The effects of diffusion capacitance and spatial hole-burning," *IEE Proceedings: Optoelectronics*, vol. 149, no. 4, pp. 182 – 188, 2002.

[40] Liu, Y., Ng, W.-C., Choquette, K., and Hess, K., "Numerical investigation of self-heating effects of oxide-confined vertical-cavity surface-emitting lasers," *IEEE Journal of Quantum Electronics*, vol. 41, no. 1, pp. 15 – 25, 2005/01/.

[41] Liu, Y., Ng, W.-C., Klein, B., and Hess, K., "Effects of the spatial nonuniformity of optical transverse modes on the modulation response of vertical-cavity surface-emitting lasers," *IEEE Journal of Quantum Electronics*, vol. 39, no. 1, pp. 99 – 108, 2003. Vertical cavity surface emitting laser;Optical transverse mode;One-dimensional rate equation model;Nonuniform optical intensity;Relaxation oscillation;Nonlinear grain suppression;.

[42] Liu, Y., Ng, W.-C., Oyafuso, F., Klein, B., and Hess, K., "Simulating the effect of spatial hole burning on the modulation response of vcsel's," vol. 4646, (San Jose, CA, United States), pp. 190 – 198, 2002.

[43] Man, W. and Yu, S.-F., "Comprehensive modeling of diffused quantum-well vertical-cavity surface-emitting lasers," *IEEE Journal of Selected Topics in Quantum Electronics*, vol. 4, no. 4, pp. 715 – 22, 1998/07/.

[44] Marcuse, D., "Classical derivation of the laser rate equation," *IEEE Journal of Quantum Electronics*, vol. QE-19, no. 8, pp. 1228 – 31, 1983/08/.

[45] Michalzik, R. and Ebeling, K., "Quasi-3d modeling of vertical-cavity surface emitting laser operation," vol. 2399, (San Jose, CA, USA), pp. 360 – 71, 1995//.

[46] Morgan, R., Lehman, J., Hibbs-Brenner, M., Liu, Y., and Bristow, J., "Vertical-cavity surface-emitting lasers: the applications," vol. 3004, (San Jose, CA, USA), pp. 91 – 103, 1997//.

[47] Odermatt, S., Witzigmann, B., and Schmithusen, B., "Harmonic balance analysis for semiconductor lasers under large-signal modulation," (Singapore), pp. 43 – 4, 2006//.

[48] Oyafuso, F., Von Allmen, P., Grupen, M., and Hess, K., "Gain calculation in a quantum well laser simulator using an eight band kmiddot;p model," vol. 6, (Tempe, AZ, USA), pp. 367 – 71, 1998//.

[49] Oyafuso, F., Klein, B., Register, L. F., and Hess, K., "Fully coupled electrical and optical simulation of vcsels," vol. 3946, (San Jose, CA, USA), pp. 108 – 116, 2000.

[50] Piprek, J., Katona, T. M., DenBaars, S. P., and Li, S., "3D simulation and analysis of AlGaN/GaN ultraviolet light-emittings diodes," in *Society of Photo-Optical Instrumentation Engineers (SPIE) Conference Series* (Stockman, S. A., Yao, H. W., and Schubert, E. F., eds.), vol. 5366 of *Society of Photo-Optical Instrumentation Engineers (SPIE) Conference Series*, pp. 127–136, June 2004.

[51] Rajan, V., "Optimality of the delaunay triangulation in R^d," *Discrete amp; Computational Geometry*, vol. 12, no. 2, pp. 189 – 202, Sept. 1994.

[52] Scharfetter, D. and Gummel, H., "Large-signal analysis of a silicon read diode oscillator," *Electron Devices, IEEE Transactions on*, vol. 16, pp. 64–77, Jan 1969.

[53] Selberherr, S., Stippel, H. H., and Strasser, E. E., eds., *Simulation of semiconductor devices and processes: Proceedings of the Fifth International Conference on Simulation of Semiconductor Devices and Processes held at the Technical University of Vienna, Austria, Sept. 7–9, 1993*, vol. 5, 1993.

[54] Shewchuk, J. R., "Constrained delaunay tetrahedralizations and provably good boundary recovery," in *In Eleventh International Meshing Roundtable*, pp. 193–204, 2002.

[55] Shewchuk, J. R., Miller, L., Civil, D. O., and Pharmaceutical, A., "Delaunay refinement mesh generation," tech. rep., 1997.

[56] Sikorski, Z., Turowski, M., Jiang, Y., Czyszanowski, T., Prezekwas, A., and Wartak, M., "Multiphysics modeling tools for vertical cavity surface emitting lasers," (Tokyo, Japan), pp. 47 – 8, 2003//.

[57] Sooudi, E., Ahmadi, V., Ebnali Heidari, M., and Soroosh, M., "Static quasi 3d thermal simulation of ion implanted vertical cavity surface emitting lasers," (Kuala Lumpur, Malaysia), pp. 244 – 8, 2007//.

[58] Streiff, M., Witzig, A., Pfeiffer, M., Royo, P., and Fichtner, W., "A comprehensive vcsel device simulator," *IEEE Journal of Selected Topics in Quantum Electronics*, vol. 9, no. 3, pp. 879 – 91, 2003/05/.

[59] Vasileska, D., Klimeck, G., and Goodnick, S. M., "Computational electronics," Jul 2008.

[60] Venkatachalam, A., Yoder, P., Klein, B., and Kulkarni, A., "Nitride band-structure model in a quantum well laser simulator," *Optical and Quantum Electronics*, vol. 40, no. 5-6, pp. 295 – 299, 2008.

[61] Verdeyen, J. T., *Laser electronics / Joseph T. Verdeyen.* Prentice-Hall, Englewood Cliffs, N.J. :, 1981.

[62] Witzigmann, B., Bregy, A., Michel, F., Odermatt, S., Santschi, R., and Streiff, M., "A full three-dimensional microscopic simulation for vertical-cavity surface-emitting lasers," (Berlin, Germany), pp. 23 – 4, 2005.

[63] Witzigmann, B., Oyafuso, F., and Hess, K., "Quasi-three-dimensional simulation of carrier dynamics in quantum well dfb lasers," *IEE Proceedings: Optoelectronics*, vol. 145, no. 6, pp. 339 – 343, 1998.

[64] Witzigmann, B., Witzig, A., and Fichtner, W., "A full 3-dimensional quantum well laser simulation," (Glasgow, UK), pp. 13 – 14, 2000.

[65] Yokouchi, N., Danner, A. J., and Choquette, K. D., "Two-dimensional photonic crystal confined vertical-cavity surface-emitting lasers," *IEEE Journal on Selected Topics in Quantum Electronics*, vol. 9, no. 5, pp. 1439 – 1445, 2003. Photonic crystals;Vertical cavity surface emitting laser (VCSEL);Lateral mode;.

VITA

Aditya Kulkarni was born to Pushpa and Ramesh Kulkarni in Belgaum, India in 1980. He received the Bachelor of Engineering degree from Sri Jayachamarajendra College of Engineering, Mysore in 2002. He then worked for four and a half years in the field of video signal processing, in particular, digital video compression, in Bangalore, India. In the spring of 2007, he started graduate work in the school of Electrical and Computer Engineering in Georgia Institute of Technology. His research inv loves efficient techniques for the simulation of laser and LED devices. He is currently working towards his Master's Degree.